Politecnico di Torino

College of Computer Engineering, Cinema and Mechatronics

Master's Degree in Mechatronic Engineering

Master's Degree Thesis

Advances in the Development of a Spherical Rover for Planetary Exploration – Part 1: Design

Supervisor:
Prof. Stefano MAURO
Dr. Matteo MELCHIORRE

Candidate:
Francesco DI STEFANO

Academic year 2023 - 2024

Abstract

The thesis focuses on the advances in the design, performance analysis and control strategy of a spherical rover actuated by a 2-dof pendulum. Designed for space exploration, the choice of rover's spherical shape offers several advantages. The presence of a continuous solid shell provides effective protection for the internal mechanism and makes the rover suitable for harsh environments, as it is immune to overturning and efficient in absorbing impacts. The design goals include the ability to move at a constant speed over 15º slope surfaces incline and to overcome 10-cm-height steps. To address the inherent limitations of the design, a gyroscope system is included. The gyroscope system provides auxiliary propulsion to the main system, allowing enhanced performances. This feature is based on the physical principle of angular momentum conservation. The work has been divided in two theses. In the following, developments concerning the revision and the re-configuration of both the mechanical and electronic design are presented.

The work starts from the previous design of a spherical rover, and considering the analysis of the state of the art. The inherited project reached a functional state. This thesis examinates and redefines the critical construction elements. Choices were made as compromise between structural reliability, transmission efficiency, and internal disposition. Positioning of system center of gravity played a fundamental role to achieve optimal performances. Subsequently, sensors and control devices were selected for the imposition of the primary and gyroscopic actuation. Signal transmission, processing efficiency, and energy consumption were considered to choose the components. Market availability and costs were deemed when selecting both mechanical and electrical components.

The structural parts have been redesigned. The final barycenter position allows optimal motion management. FEM analyses were made for the sizing of the elements in various load conditions, satisfying design requirements have been met. The results of this part of the work culminate in a rover design suitable for prototyping.

Contents

List of Tables

List of Figures

List of Abbreviations

ROV	Remotely Operated Vehicle
UGV	Unmanned Ground Vehicle
SAR	Search and Rescue
SMR	Spherical Mobile Robots
BCO	Barycenter Offset
BSR	Barycenter Spherical Robot
SR	Spherical Robot
IDU	Internal Driving Unit
PID	Propotional-Integrative-Derivative
DOF	Degrees of Freedom
CMG	Control Moment Gyroscope
COAM	Conservation of Angular Momentum
IMU	Inertial Measurement Unit
MCU	MicroController Unit
COM	Center of Mass
SW	SolidWorks

SPI Serial Peripheral Interface

Chapter 1

Introduction

Spherical robots (SRs) are of significant importance within the context of mobile robotics, offering a number of advantages over their traditional counterparts, including wheeled and legged robots. Their geometry prevents them from tipping over and provides high resistance from impacts. Furthermore, the shell protects the internal components from contaminations and other possible environmental danger. The symmetrical design always allows the rover to regain control and to actuate fluid and responsive movements. Another important feature that characterises them is the energy saving in case of downhill movements. Furthermore, depending on their drive mechanisms, some SRs can achieve omnidirectional movement.

For the reasons listed above, spherical rovers represent a class with great technological and applicative potential. Being resistant to contamination and impact allows their use in search and rescue situations. Their robustness facilitates surveillance operations in difficult-to-access territories. Specific categories of Spherical Rovers are employed for use in underwater environments, as their shape allows them to be highly resistant to pressure. Several applications have been developed for data collection, environment monitoring and surveillance. Finally, they can be of considerable contribution to the branch of space exploration. Recent space programmes for the Moon and Mars have led to an increase in the interest of space companies in such technologies.

Although the geometry is a distinctive feature, spherical rovers can be divided into multiple categories. The main difference that characterises them is the actuation of motion. Among the most well-known examples are hamsterballs, which feature an internal counterweight by which motion is generated. Fundamental differences between the categories are in their performance. Hamsterballs present themselves as rovers that are easier to control than pendulum-driven. However, the second ones are more effective for a wide variety of situations. This sector is therefore characterised by different approaches depending on the objectives to be achieved by the project.

In this thesis work, advances concerning the design and control system of a spherical rover are presented. The project examined is based on the work of M. Melchiorre and T. Colamartino. In the study by M. Melchiorre et al., the development of an Unmanned Ground Vehicle (UGV) [1] was addressed. Through a trade-off analysis, the project developed led to the definition of a prototype spherical rover with barycenter offset propulsion. The motion transmission principle and the main structure of the rover were defined. In particular, the pendulum has two degrees of freedom, enabling the rover to navigate curved trajectories. Kinematic of the differential system and dynamic formulas of the shell were defined and a control system was constructed to manoeuvre the rover.
Finally, the project objective were defined as follows:

Table 1.1: Design objective of [1].

Max. Step Height	$25mm$
Max. Slope Angle	$15°$
Min. Velocity	$2.5m/s$
Min. Acceleration	$0.5m/s^2$
Max Diameter	$0.5m$
Max Mass	$25kg$

Although the design performed well for control, the structure had some limitations for versatility and efficiency. One of the main points was the inability to achieve high torque values for overcoming obstacles.
The work carried out by T. Colamartino resulted in singnificant contributions in the design and control management of the rover. The greatest contribution can be found in the integration of two Control Moment Gyroscope (CMG), through which the slope climbing and the obstacle overcoming capabilities were increased. Through the principle of gyroscopic moment conservation, it is possible to provide a boost to the torque acting on the shell for overcoming steps up to $10cm$ in height. The equations

linking gyroscopic actuation to obstacle overcoming have been derived and the main actuation components have been dimensioned.
Based on the 2D equations of dynamics, T. Colamartino developed a control system to manage rectilinear motion. By implementing a Fuzzy Propotional-Integrative-Derivative (PID), the rover is able to faithfully follow speed profiles. Tests were carried out for step climbing too.

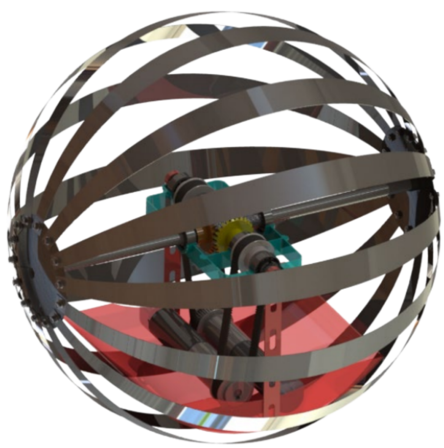

Figure 1.1: SR designed by M. Melchiorre.

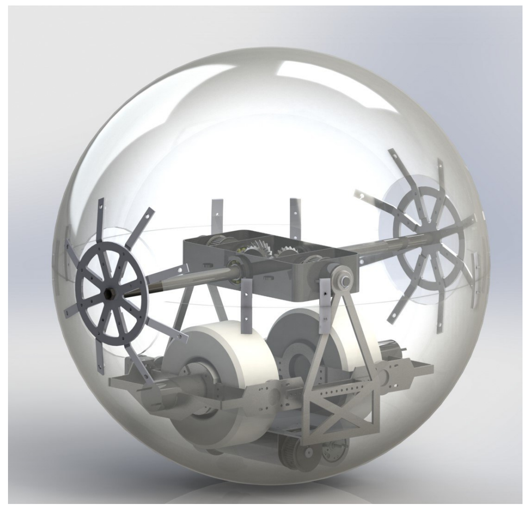

Figure 1.2: SR designed by T. Colamartino.

This work presents the advances developed based on the design elaborated by Tommaso [2]. Although the rover had a well-defined design, no considerations were made from a constructional point of view.
The advances obtained as a result of the thesis have been divided into two parts. This is the first part and aims at explaining the considerations regarding the final elaborated design, which is suitable for prototypation. Studies on weight, overall dimensions and internal force distribution were carried out. Electronic selections is addressed, by considering the required measures and actuation needed for an effective control strategy.
The second part focuses on the performance analysis and the required power supply. Then, advances obtained with respect to the modelling of the plant and the development of planar control systems to manage the rover motion are reported.

1.1 Project Objectives

The aim of the thesis was to refine the components that make up the structure of the rover in detail, to guarantee operability without damage. The previous project presented an innovative way of defining the implementation. However, the resulting design and performance presented assumptions that had to be coincided with physical structural limitations of the rover. Since the performance of the rover depends on the weight distribution and thus the geometry of the structure, it was necessary to identify the main points to achieve a trade-off between operability and feasibility of the supporting structure.
The final system must be able to acquire position and speed information to implement control strategy. Ideally, the objective is to derive a rover autonomous in driving. A major limitation of the design is the large amount of unusable space. In fact, since the pendulum structure is in constant rotation relative to the shell, the positioning of additional components is challenging. Choices must also be made in order to maintain high energy efficiency while keeping the centre of gravity of the system as low as possible to ensure that obstacles can be overcome.
Developing a control system that can manoeuvre the rover in planar space remains a key objective. Since the rover is equipped with a 2-Degrees of Freedom (DOF) pendulum, it is necessary to implement a lateral angle control in order to define curvilinear trajectories. The presence of a forward position control only does not allow to fully implement the rover capabilities.

1.2 Contribution of this work

The thesis work presents a major contribution to the development and realisation of a prototypable model of a SR 2-DOF pendulum driven and the implementation of different control strategies. Work contributions can be resumed as follows:

- Comprehensive state-of-art to indviduate the fundamentals of the proposed work
- Design review. Identification of the system's failure points and dimensioning that takes into account the various working states of the system. Modifications must take into account the positioning of the centre of mass so as not to alter

the performance of the system. The work can be considered as an estimate for production. Electronic components were defined for the implementation of a control system. In addition, the layout was chosen so that the movement of the various internal components would not be obstructed.

- Development of a 3D analytical model using Euler-Lagrange equations
- Development of a lateral model capable of exploiting the second degree of freedom. Subsequently, integration of the lateral control to the forward control for complete rover motion management. Different control algorithms were developed to test performances in several situations. Comparisons between management by separate and merged controls are rare in the literature, this work explores the possible cases.

The presented study is the result of a larger thesis project. Design aspects that have been anticipated are discussed with in detail in this paper. Developments concerning the modelling and control of the rover are covered in Part 2.

Chapter 2

State of art

2.1 Introduction to State of Art

Spherical robots are highly significant in the field of mobile robotics due to their numerous advantages over traditional wheeled and legged robots. Their spherical casing protects internal components from contaminants such as water and dust, as well as from impacts. Additionally, the symmetrical design ensures the robot cannot overturn, allowing it to withstand falls and be propelled over obstacles without risk of damage or flipping. The spherical shape also enables the robot to roll down slopes without energy consumption. Furthermore, certain spherical robots can achieve omnidirectional movement, depending on their driving mechanism.

Despite these numerous advantages, this class of mobile robots also has some disadvantages: they typically generate a limited maximum torque, their performance in climbing obstacles and navigating steep terrains is constrained, and positioning external sensors is challenging. Nevertheless, the benefits of spherical robots make them excellent candidates for a wide variety of applications. They are primarily designed for exploring unstructured, harsh, and hostile environments such as planets, caves, and pipes. Moreover, they can be used for: inspecting disaster areas to evaluate damage and potential hazards, conducting Search and Rescue (SAR) operations, performing underwater inspections, data collection, and environmental monitoring. Finally, implementation for social services as surveillance, indoor exploration, and child monitoring have been derived.

The following sections presents the current state-of-the-art overview of Spherical Mobile Robots (SMR), focusing on the most common driving mechanisms developed to date and highlighting some of the latest research papers on this topic.

2.2 Spherical mobile robot classification

A comprehensive account of the technological advancements on spherical rover, including both established and novel developments, is presented. Several papers that bring innovation to the subject field are accounted for this scope.
The spherical robot could be classified in many different aspects. The first and most important is the driving mechanism and locomotion. A secondary classification could be done depending on the Applications, or also based on the different Control system proposed and Sensors implemented. A scheme was derived, Figure 2.1, to describe the most popular and studied mechanisms inside the spherical robots.

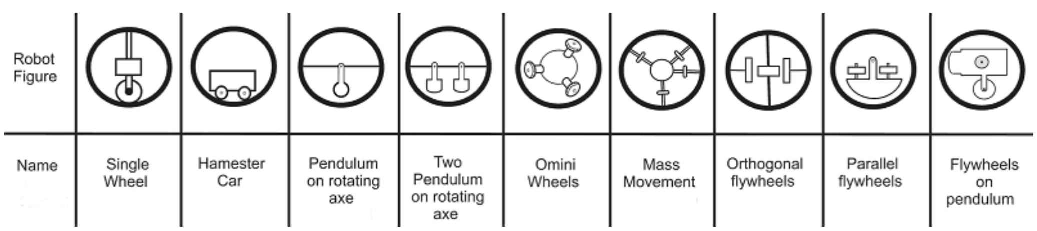

Figure 2.1: Spherical rovers more known models [3].

2.3 Barycenter offset actuation

The most popular studied spherical robot group is by far the class of Barycenter Spherical Robot (BSR), viewable from Figure2.2.
The concept of barycenter-actuated spherical robots involves a unique mechanism where the robot's movement is controlled by shifting its internal mass, effectively changing its center of gravity. This allows the robot to roll in the desired direction by strategically repositioning the internal mass to create a rolling motion.

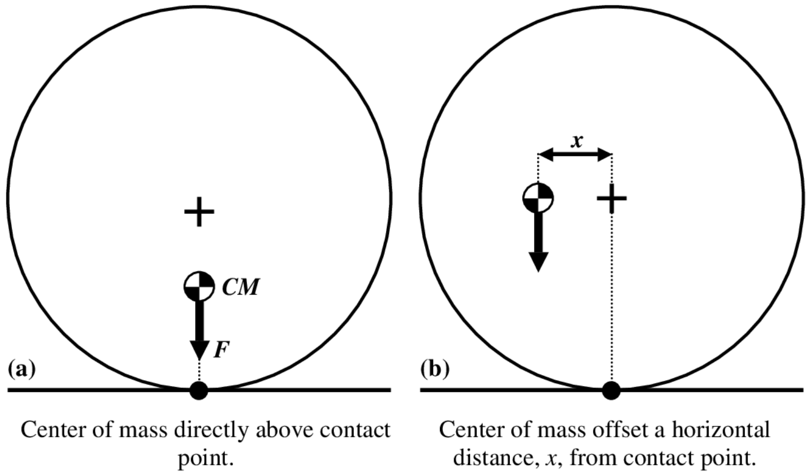

Figure 2.2: Barycenter offset actuation.

Barycenter-actuated spherical robots represent an innovative approach to mobile robotics, leveraging internal mass shifts to achieve movement and stability. Their design makes them ideal for a wide range of applications, particularly in environments that are challenging for traditional robots. However, they also come with design and operational complexities that need to be addressed.

The BCO SR category mainly contain 3 typology of actuation, that are: the Pendulum driven, the Internal Driving Unit (IDU), and the Sliding Mass.

2.3.1 Pendulum-driven

The core mechanism in this typology of BCO-SMRs involves a pendulum that is free to swing inside the spherical shell. By moving the pendulum, the robot shifts its center of gravity, causing the sphere to roll in the desired direction. The movement of the pendulum needs to be precisely controlled to direct the robot's rolling motion accurately. By adjusting the pendulum's angle and the speed of its movement, the robot can achieve forward, backward, and turning motions. The dynamics of the pendulum are crucial for maintaining stability and ensuring smooth movement.

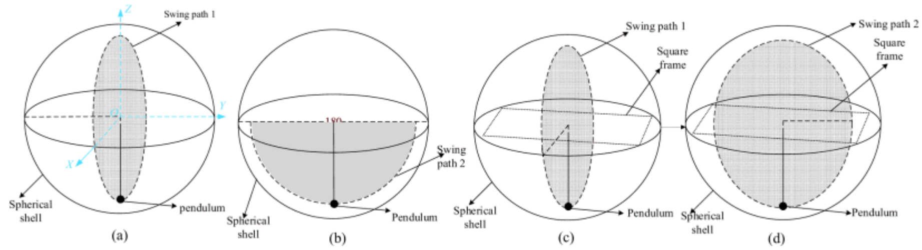

Figure 2.3: 2-DOF pendulum-driven SMR main movements [4].

For example Sneha Gajbhiye et al.in 2015 [5] shows the design and realization of a spherical robot in which the inner mechanism exploit a pendulum for the straight motion and an hollow bar called yoke for steering. A Lagrangian approach with non-holonomic constraints is used for the dynamics computation, finally developing a local equilibrium control system.

Another example of this SR typology came from Roozegar, Mehdi et al (2017) [6]; where a 2-DOF pendulum driven robot is developed, it has $40mm$ diameter shell and provided by two stepper motors to actuate it, all controlled by a Fuzzy PID and cameras sensors.

Animesh Singhal et al.(2022) [7] worked on a spherical robot with a platform housing the yoke for sideway movement and pendulum for the forward one. Nonlinear dynamics is treated by using Lagrange-D'Alambert equations. Control strategy for the yoke is addressed by means of PD controller, to quickly settle the side angle to a desired value. Pendulum controller implements Tp to counter-act gravity torque through a feedforward term.
A speed controller is designed too. Using torque as input and a feedback term, a proportional controller allows to impose starting forward velocity.

During Seeman, Mattias et al. research (2006) [8] a pendulum-driven robot was used to study the autonomy of a surveillance robot. The study highlighted several advantages of spherical robots, such as their stability and robustness, but also identified some drawbacks, like difficulties in image stabilization due to uncontrolled oscillations.

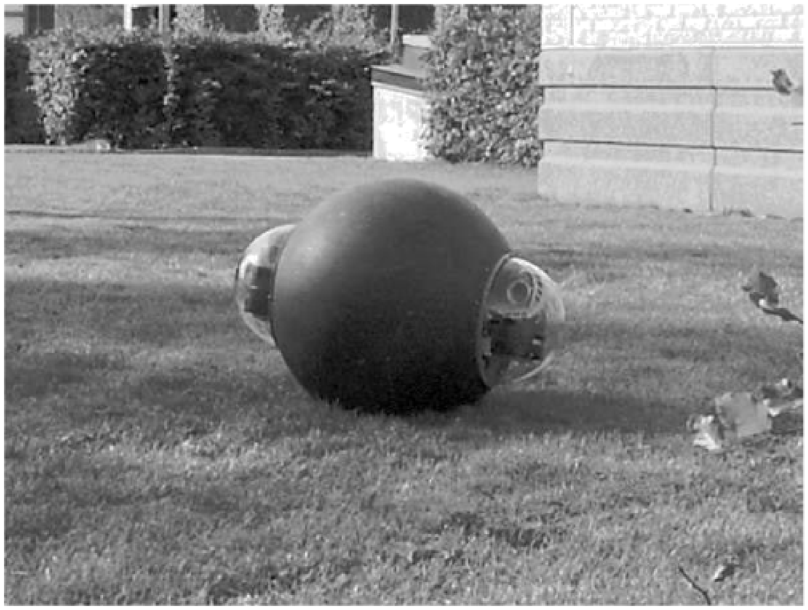

Figure 2.4: GroundBot [8]

GroundBot (Figure 2.4), despite being one of the best in its category, has some limitations in overcoming obstacles due to its driving mechanism.

The study made by Yang, Maotao et al.(2020) [4] focused about the design of a 2 DOF pendulum robot with a shell, a square frame, a control module, a drive unit, and the pendulum. Two separate motors manage the forward and lateral movement of the Remotely Operated Vehicle (ROV). Finally a simplified dynamics is developed, based on Lagrange equations, and straight motion experiment shows a small deviation due to eccentric masses.

DEDALUS Sphere robot [9] represent an hybrid pendulum-actuated rolling robot able to shape trasformarm and with the ability of extend a pair of poles in order to avoid obstacles. Primarily studies has been made with a prototype construction to demonstrate also the high compatibility of this typology of robot for planetary surfaces.

An interesting example from literature combine a pendulum driven spherical robot connected to an half hemisphere, while a jumping module is innested to the other half hemisphere [10]. After deriving the Lagrangian dynamics, the experimental tests shown the capabilities of the robot, like 170mm of jumping height and 150mm of steering radius.

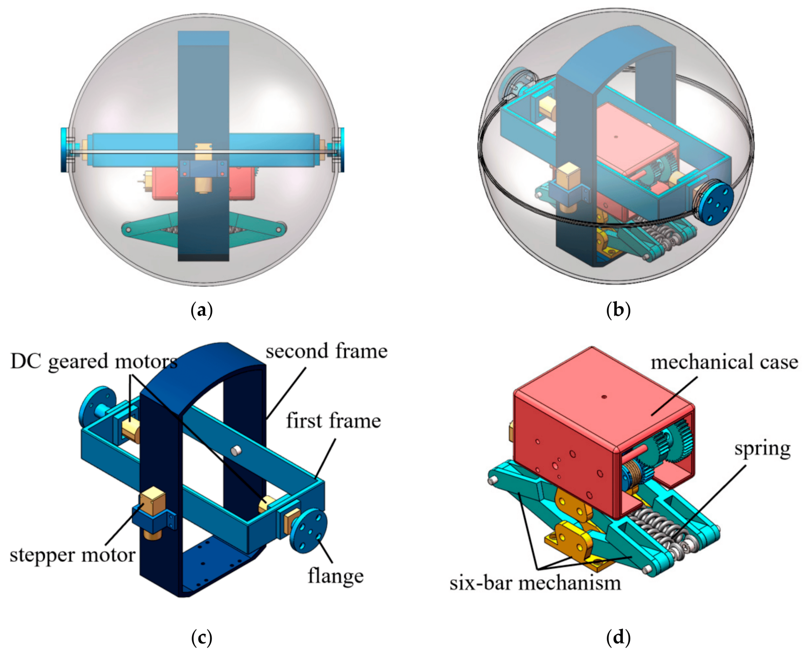

Figure 2.5: (a) The front view of the rolling and jumping spherical robot. (b) The isometric view of a rolling and jumping spherical robot. (c) The rolling driving module of the spherical robot. (d) The jumping driving module of the spherical robot [10]

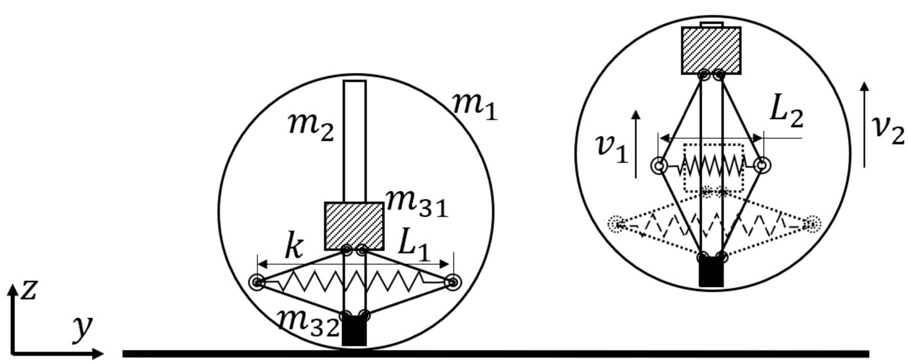

Figure 2.6: The simplified scheme of the jumping of a spherical robot [10]

Another notable review by Bo Zhao et al.(2010) [11] consist of developing this type of spherical robot that specifically features semi-omnidirectional movement 2.7. By synchronously rotating two pendulums in opposite directions, the robot generates an inertial moment around the yaw axis, allowing it to turn in place with precision, which makes it suitable for reconnaissance purposes and also for exploring unstructured and hostile environments.

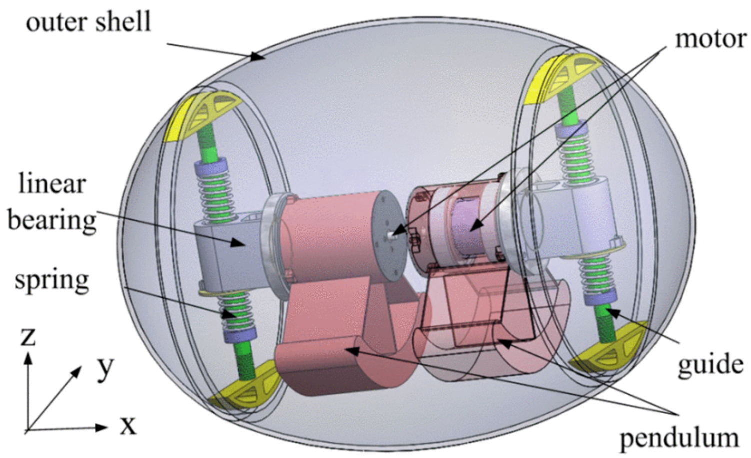

Figure 2.7: Mechanical structure of the robot of Bo Zhao et al.

2.3.2 IDU or Hamster ball

The IDU spherical robots represent a specialized category of spherical robots that utilize an inertial drive mechanism for movement. The hamster ball driving system consists of a multi/single wheeled mobile robot placed inside the spherical shell that climbs up the internal surface of the sphere, causing the barycenter displacement towards the desired direction.

This system has several advantages: the barycenter is closer to the shell surface with respect to a pendulum driven system, which allows maximizing the output torque. The design is simple, and the driving mechanism is straightforward to control. In some hamster-ball-driven spherical robots, the IDU is kept in place through a tensioning element, that is usually a platform or a rod with a wheel placed at the top. The introduction of the tensioning element is important for preventing the IDU from slipping or overturning.

One of the biggest problems of this system is that the internal surface of the sphere needs to be as uniform as possible to maintain the friction between the IDU wheels and the shell. Collisions with obstacles could cause the loss of contact between wheels and internal surface and the overturning of the robot in the worst case. The omnidirectionality of the robot depends on the type of wheels of the IDU. The most recent developed hamster-ball-driven robots are characterized by omni wheels, which allow omnidirectional movements.

BHQ-3 developed by Qiang Zhan et al.(2011) [12] is one of the most emblematic Hamster ball, able to roll over an inclined plane of 17 degrees slope and overtake 3 cm obstacles, with a 150mm radius spherical shell.
BHQ-3 shows an IDU composed by 2 main wheels, one for the main movement, the other one for steering purpose changing the direction of the previous wheel. After the kinematics computation and the controllability analysis, it was demonstrated that the prototype was able to perform the desired trajectory from radio-control input and also handle manoeuvre over water.

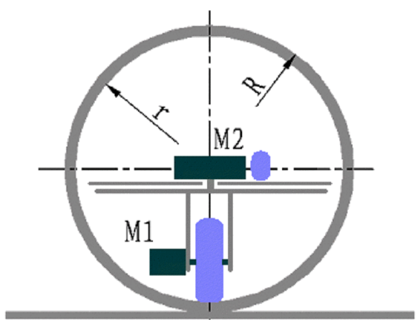

Model of linear motion of BHQ-3.

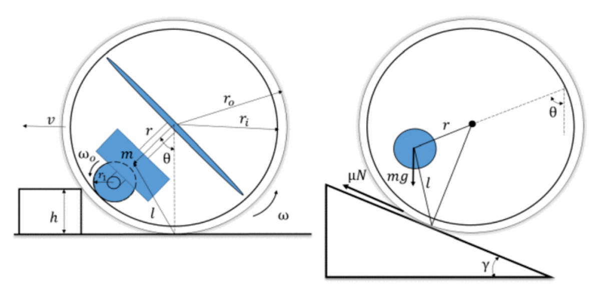

Obstacle overrun and uphill climbing.

Figure 2.8: BHQ-3 overview

The previous work inspired another case study by Singh, Akash et al. (2018) [13], where is presented a snake robot composed by 3 BHQ-3 Spherical robot.

Chen, Jiazhen et al. (2016) [14] designed the robot in Figure 2.9 with an internal driving unit composed by the straight motion with a contact wheel, the steering mechanism and finally a CMG group.
After the design part, a set of simulations showing the robot trajectory by algorithm.

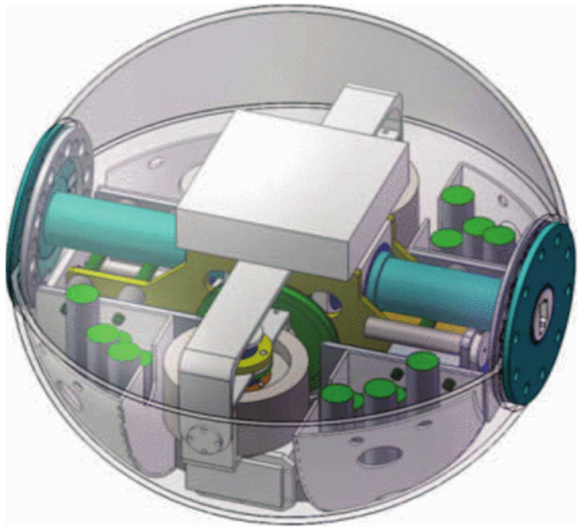

Figure 2.9: Spherical robot with CMG.

2.3.3 Sliding mass

This system comprises multiple masses capable of linear displacement within the robot along fixed linear guides. Unlike the pendulum driving approach, it enables omnidirectional movements and offers more precise control over the barycenter position. However, its mechanical design and required control architecture are highly intricate. Additionally, the system's efficiency is compromised due to the necessity for high-power actuators to achieve faster and smoother movements. Furthermore, collisions at the attachment points of the linear guides to the shell are deemed undesirable.

One example came from Sang, Shengju et al. (2010) [15] in Figure 2.10). The related paper deals with the study of a spherical robot made by an acrylic sphere of $360mm$ radius and four power screwed spokes placed at tetrahedron as actuation system.
All the components are symmetrycally implemented in order to preserve a central barycenter and to avoid that the robot tip over itself.

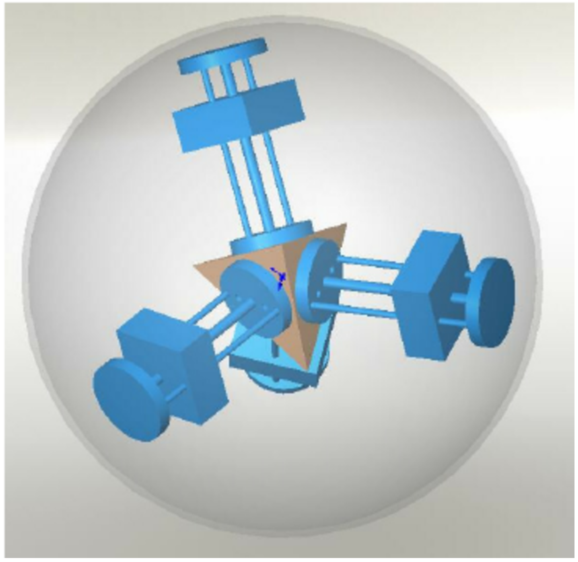

Figure 2.10: Prototype of the spherical robot [15]

2.3.4 Other

There are also many other spherical robot designs that exploit different kind of actuation with the same BCO physical principle.

Emblematic example came from [3], where S.A. Tafrishi et al.(2016) developed a unique driving system for a spherical mobile robot actuated by fluid. Their study focuses on a design featuring an internal network of pipes through which an incompressible fluid is propelled by a hydraulic mechanism. The movement of this fluid creates the necessary force to drive the robot. Within this piping system, there are specific sections responsible for controlling forward (pitch) and side-to-side (roll) movements. A significant advantage of this innovative actuation method is that it eliminates the unstable points commonly found in pendulum-like systems. The rover is shown in Figure 2.11.

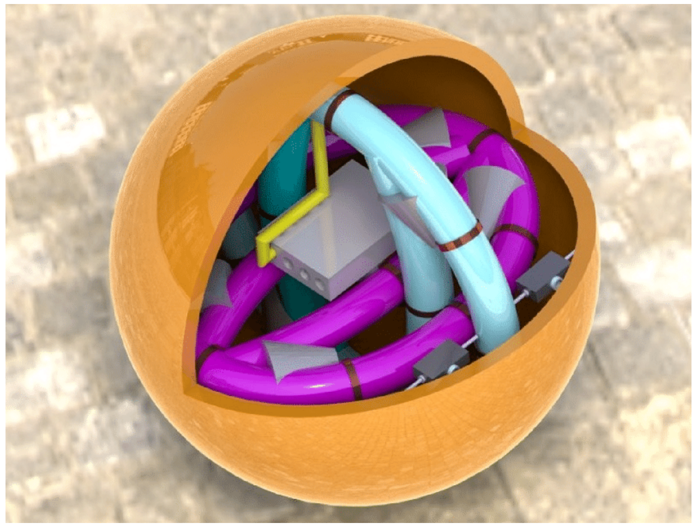

Figure 2.11: Rover developed from S.A. Tafrishi et al.

L. Jia et al.(2016) [16] developed the amphibious spherical robot in Figure 2.12, capable of underwater navigation and autonomous movement toward the water using a dual inverted pendulum mechanism. The robot features a spherical shell housing the batteries, payloads, three DC motors, and the control board. Two arms extend from the sides of the hull, each equipped with a propeller at the end. The robot achieves rolling motion by shifting its center of gravity with the arms acting as inverted pendulums. To change direction, a small flywheel inside the shell rotates, creating a reaction force that alters the yaw angle (Conservation of Angular Momentum (COAM) driving mechanism). The propellers at the arms' ends facilitate underwater navigation. Additionally, two small grippers next to the motors enable manipulation tasks.

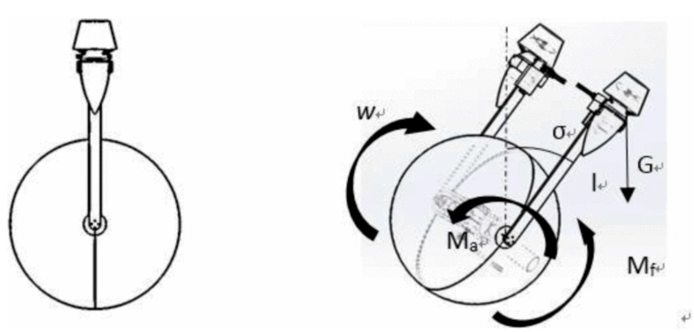

Figure 2.12: "RollRoller", spherical mobile robot [16]

2.4 Shape Trasformation

Spherical robots with shape transformation can be categorized into two groups, each employing distinct propulsion strategies: shell deformation and hybrid mechanisms. Shell deformation involves altering the spherical shape to generate driving force, while hybrid robots can alter their structure to switch propulsion methods. Among these, hybrid robots are more prevalent, featuring various mechanisms enabling both rolling and other types of movement, as documented in literature.
The primary advantage of shape transformation, lies in significantly enhancing the robot's ability to traverse obstacles while retaining the benefits of a spherical shape. However, the mechanical design and control architecture of such robots are considerably more complex. The following paragraphs provide examples of crawling and rolling, flying and rolling, amphibious, and soft inflatable spherical robots.

2.4.1 Crawling and rolling

These robots are distinguished by their capacity for both walking and rolling. They can operate in a closed configuration, utilizing rolling motion for energy-efficient travel, or extend their legs to crawl. Their walking capability enhances obstacle traversal and addresses the limited maximum torque challenge faced by pendulum and hamster-ball driven spherical robots.

S. Kamon et al. (2021) [17] developed a crawling robot. This robot features three legs that are stored within two hemispherical shells. The legs extend by splitting the top half of the spherical shell using a linear actuator located at the core. Each leg comprises three revolute joints. On the ground, the robot can execute two types of walking gaits: the crawl-kick gait (with one leg in front and two legs at the back) and the butterfly gait (with two legs in front and one leg at the back). On flat surfaces, the robot achieves a speed of $5.33cm/s$ with the butterfly gait and $6.15cm/s$ with the crawl-kick gait. It can also navigate small obstacles at $1.57cm/s$ and $1.51cm/s$ for the butterfly and crawl-kick gaits, respectively.

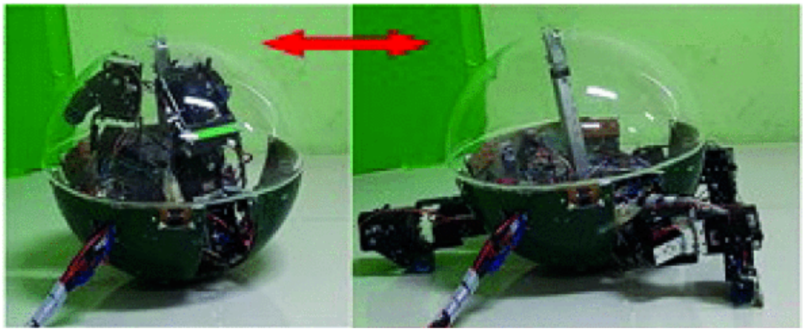

Figure 2.13: Crawling robot of S. Kamon et al.

T. Aoki et al.(2020) [18] have introduced and developed a novel quadruped walking robot with a spherical shell, named “QRoSS”. “QRoSS” is a transformable robot capable of retracting its legs into its spherical shell. This shell not only absorbs external forces from all directions but also enhances mobility due to its rounded shape. In disaster site rescue operations, transporting robots into the site poses a danger to operators, potentially causing secondary accidents. With QRoSS, robots can be safely and easily deployed by being thrown into the site rather than carried. A different set of performance test has been made in order to check the ability of landing, rising and walking.

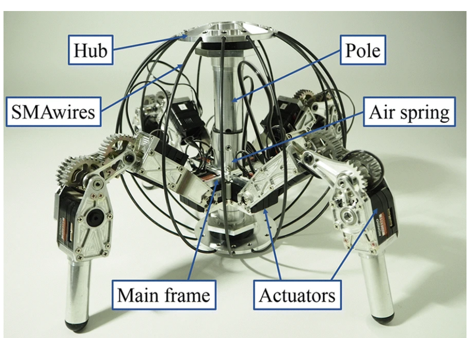

Overview of the structure.

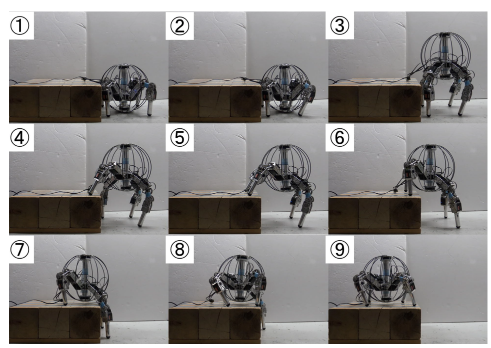

Climbing over a step 120mm high

Figure 2.14: QRoSS structure and performance

J. Pan et al.(2019) [19] created a soft spherical robot prototype, taking inspiration from the modularity and functions of organisms such as starfish and octopuses. This robot features two hemispherical shells made with 3D printing, which are joined together by electromagnets. Each hemisphere is equipped with five silicone gel feet, controlled by SMA springs, two per foot. These feet enable the robot to crawl and, when closed into a spherical shape, to roll. Moreover, the hemispheres can detach and operate independently, allowing the robot to maneuver through tight spaces and overcome obstacles.

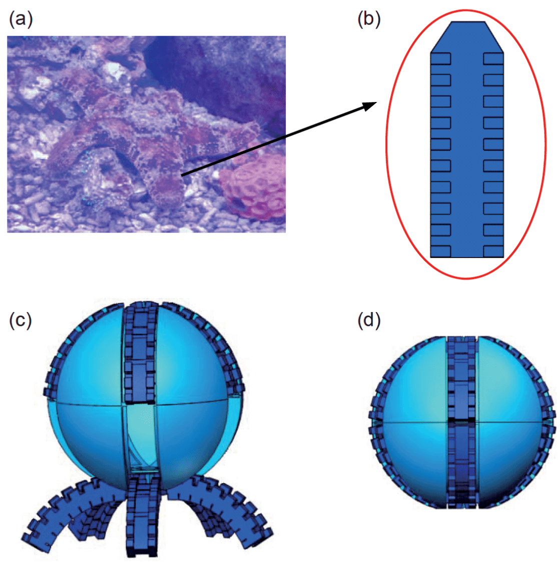

Figure 2.15: (a)Starfish shape, (b)Robotic foot, (c)Crawling mode, (d)Sphere shape

2.4.2 Amphibious spherical robot

This category of spherical robots includes all the ones that are designed to move on land and navigate underwater.
In their paper, Li M. et al.(2014) [20] introduced an innovative amphibious robot with a spherical design that enables both quadrupedal walking on land and underwater navigation via a water-jet propulsion system. The robot's structure includes a reconfigurable shell that opens at the bottom for terrestrial movement. This spherical form was selected to maximize internal volume, ensure symmetry for efficient movement in both environments, and facilitate navigation in tight spaces. Inside the shell, it carries various micro-robots designed for tasks such as underwater object collection, manipulation, and environmental monitoring in confined areas.

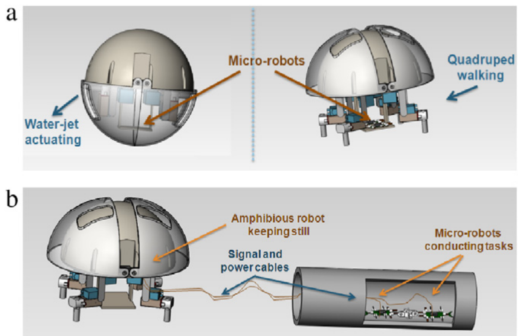

Close target movement.

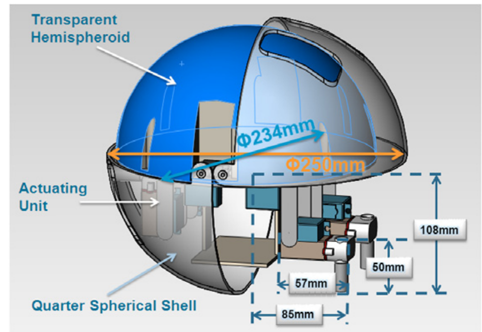

Robot structure.

Figure 2.16: Amphibious robot design.

2.4.3 Soft inflatable robots

Among the spherical robots characterized by the ability of transforming their shape, some inflatable robots can be found.
In one review Ho, Kuan-Yi et al. (2017) [21] designed the inflatable robot, able to get a spherical shape exploiting an internal pneumatic system to control the pressure; many different robot areas can be inflated. For this particular conformation, the rolling motion is possible thanks to the actuation and so the inflation of specific robot areas.

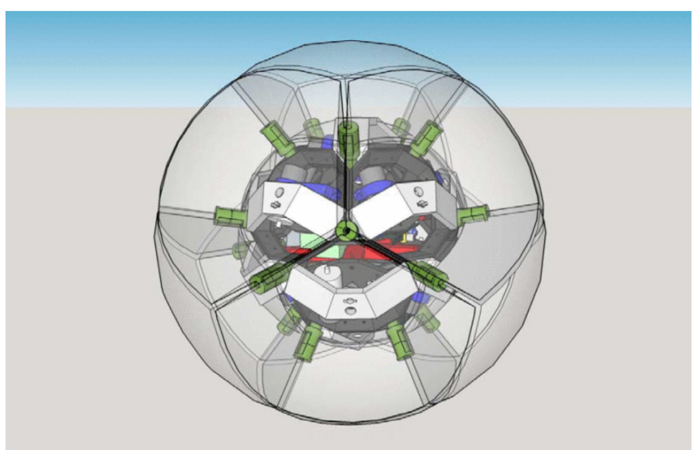

Figure 2.17: Overview of inflatable robot.

2.5 COAM

The principle behind the actuation of this kind of robot is the "Angular moment conservation", it is practically based on a mass spinning at high angular velocity around an axis and then tilting it around a second one; the final result consist of a torque generated in the third direction which tries to re-set the mass at the unperturbed rotation around the first axis. This principle is used in spherical robot mainly because the mechanism could create a boost action able to over-impose physical limitation of the robot, or also is employed for the driving system.

2.5.1 CMG

One of the most famous Spherical robot is the one developed by Schroll et al. (2007) [22] in Figure 2.18, introducing an hybrid robot capable of motion thanks to the 2 DOF pendulum. In addition the principle of conservation of angular moment is used for boosting purpose by two set of control moment gyroscope.
The developed prototype has a $0.46m$ diameter sphere and $15kg$ mass. Althought the wobble behaviour and the oscillation back and fourth, the robot is able to overcome a $10cm$ obstacle using the $2.2kg$ CMG couple spinning at $10000rpm$ reaching an angular momentum of $10Nm\,s$.

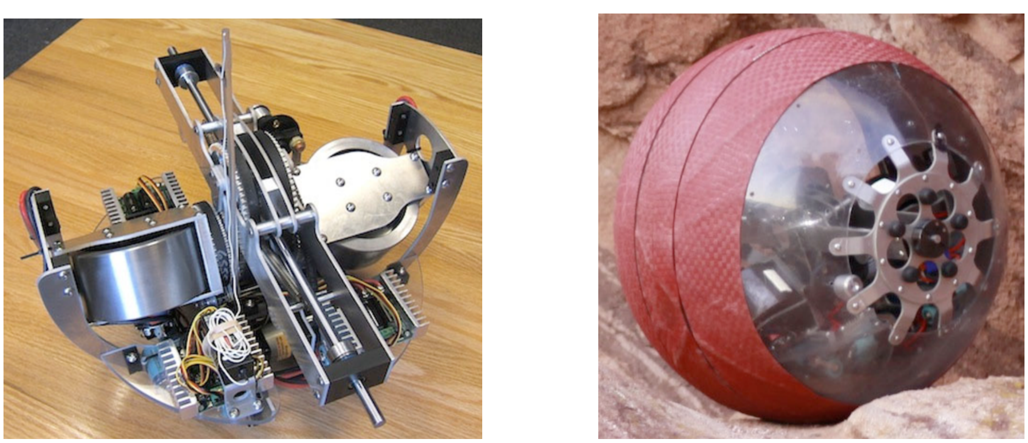

Internal actuation. Complete robot structure.

Figure 2.18: Schroll et al. rover.

Lee, Jaeyeon et al.(2009) [23] in the related review take into account the study of an omni-directional SR with a high spinning flywheel. In this setup, the flywheel fulfills two roles: facilitating forward motion and altering the robot's heading direction. A third motor is dedicated to spinning the rotor, thereby increasing the robot's angular momentum. The pose of the robot is estimated using a Kalman Filter, which processes data from the IMU and motor drivers. Additionally, sensors monitor the flywheel's lean angles and spin rates.

2.5.2 Reacting Wheel

Qingxuan, Jia et al. (2009) [24] introduces the BYQ-V, a spherical robot that leverages the gyroscopic effects of a high-rate flywheel to enhance stability. The gyroscopic phenomenon of the flywheel plays a crucial role in stabilizing the robot. The omni-directional robot is made by a spherical glass shell of $600mm$ radius and about $25kg$ mass with inside a simil-yoke with the flywheel below it. The dynamic equations are formulated and simplified based on certain assumptions that lead to the design of a Linear Quadratic Regulator (LQR) controller and a Proportional-Derivative (PD) controller for the robot. Both simulation and experimental results are finally presented, demonstrating the effectiveness and validity of the proposed controllers.
The rover is shown in the figure blow.

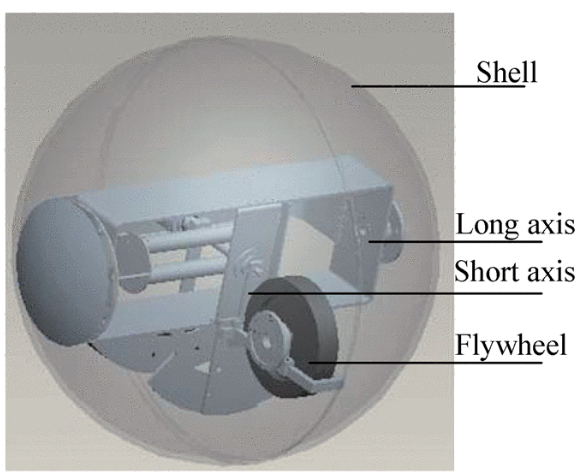

Figure 2.19: Model of BYQ-V.

2.5.3 Differential driving systems

In 2020, E. V. Potapov et al.[25] developed two similar prototypes of differential-driven spherical mobile robots designed to explore indoor environments and recognize objects using computer vision algorithms (Figure 2.20). These robots house batteries, motors, microprocessors, and cameras on a central platform. The small motors enable the prototypes to maintain a steady speed of $0.26 m/s$.

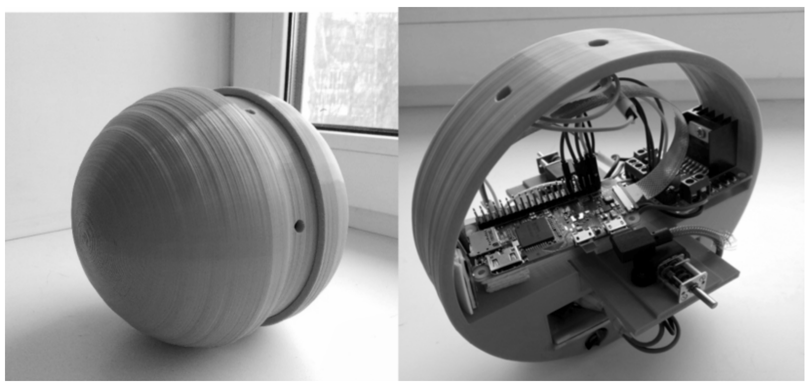

Figure 2.20: External and internal view of spherical robot.

The design of RolLeapO [26] employs two semi-spheres for rolling. By varying the speeds of the two semi-spheres, the robot can turn effectively. This configuration does not occupy much internal space, allowing for the middle area between the semi-spheres to remain free. This space facilitates the installation of the leaping mechanism and the energy storage device. The leaping mechanism of the robot incorporates a five-bar linkage with an integrated inner spring serving as the energy storage device. A spur gear pair is attached to the lower two linkages, ensuring that the left and right movable linkages operate symmetrically. The DOF of the five-bar linkage is managed by a release/retract mechanism controlled by a string. Upon releasing the string, the spring contracts, pushing the five-bar linkage out of the spherical shells and propelling the robot into a leap.

Y. Dong et al. [27] developed a spherical robot capable of both rolling and jumping, the robot features two independently rotating hemispherical shells. A support pedestal situated between the shells houses two brushless motors and the jumping mechanism. This mechanism utilizes a spring to store elastic potential energy, which is released to help the robot overcome obstacles. The prototype created by the authors demonstrated the ability to jump up to $58cm$ with a take-off angle of $60°$ during tests, as can be seen in Figure 2.21.

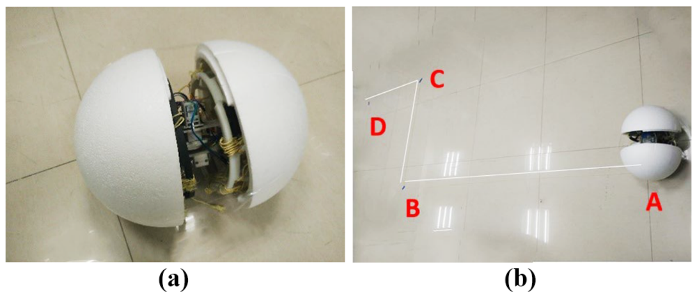

Figure 2.21: (a)Prototype of the robot, (b)Motion experiments

2.6 Other Spherical robot

C. J. Dudley et al. (2015) [28] introduced a prototype of a micro spherical robot capable of both rolling and flying.

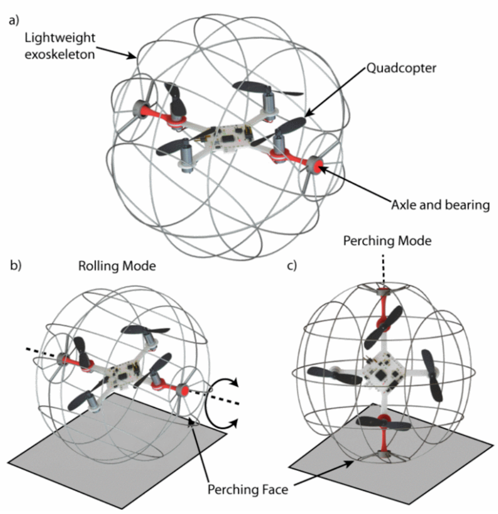

Figure 2.22: (a)Key components, (b)Rolling mode, (c)Perching mode.

This design features a "micro-quadcopter enclosed within a lightweight spherical exoskeleton that can rotate around the quadcopter." By combining these two modes of movement, the robot achieves greater versatility, allowing it to easily overcome obstacles, navigate tight spaces, and utilize rolling for more efficient travel compared to robots that flying only robot.

S. Sabet et al.(2019) [29] introduced Rollcopter in Figure 2.23, a spherical mobile robot that integrates both rolling and flying capabilities. This innovative design features six reversible propellers aligned along three orthogonal axes, enabling the robot to fly in any orientation and generate the torques necessary for rolling. Simulation results indicated that the force required for rolling is less than that needed for flying. However, the advantage of rolling diminishes as the translational velocity or slope increases, with the forces becoming equal at a 90° slope i.e. in vertical ascension.

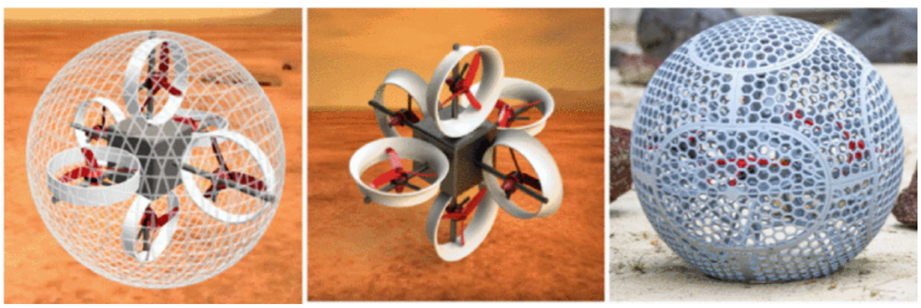

Figure 2.23: : Left: Rollocopter concept art, including propellers, electronics (gray box) and the impact-resilient cage. Middle: hexacopter configuration of the propellers. Right: A Rollocopter prototype. The spherical cage allows to roll on flat terrains and to be impact-resistant, while the configuration of the propellers guarantees actuation in any direction.

Shi, Liwei et al. (2020) [30] developed a small bionic amphibious spherical robot system for tasks such as coastal environment monitoring and offshore autonomous search and rescue. It mainly use a Fuzzy PID control algorithm to design an underwater motion control system and it was also carried out experiments on the three-dimensional (3D) motion control to validate the design of the underwater motion control system. Althought the robot skills are pretty limited it show a great reliability in control.

Li T. and Liu W. [31] developed a wind-driven spherical robot with a unique collapsible structure. This robot can transition between a folded state and an inflated state, allowing it to travel using various movement modes: rolling, bouncing, and flying.

The level of inflation determines its preferred mode of navigation, with different degrees of inflation favoring different types of movement.

Gu, Shuoxin et al.(2020) [32] designed a spherical 460mm diameter underwater robot (SUR IV) with hybrid propulsion devices including vectored water-jet and propeller thrusters (Figure 2.24). This kind of high and low speed hybrid propulsion mode can not only save the detection time and improve the work efficiency, but also can improve the detection precision and accuracy when slowly approaching the target.

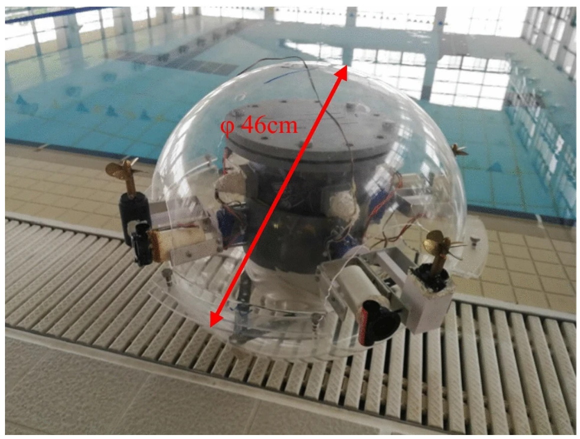

Figure 2.24: The prototype of SUR IV.

Chapter 3

Previous Work

The study and development of the spherical rover in question, begins from the original conception by M. Melchiorre in literature [1].
M. Melchiorre performed a detailed exposition of the design of a personal prototype of a spherical rover, by analyzing its various aspects. The work includes its physical behaviour, actuation mechanism, components, analytical model and a multibody representation in Simulink/Simscape domain.
In the thesis carried out by T. Colamartino [2], the initial design is resumed and expanded by the implementation of two CMG. The final result is a original conception of SR that combines pendulum-driven actuation with the benefits of a gyroscopic torque as boost to overcome obstacles. The system was validated by means of multibody simulations and a controller controller for linear speed profiles was derived.

3.1 Melchiorre's Thesis

The rover originally intended, consisted of a pendulum actuated Barycenter Offset (BCO) capable of exploring multiple territories (including the lunar surface) and overcoming obstacles of $25mm$ height or less or inclined planes with a $15°$ slope.
The prototype is equipped with two DC motors placed at the bottom of the pendulum. Transmission is carried through pulleys and belts to lateral shafts of a differential mechanism. The differential mechanism has three bevel wheels as the main mechanism actors. The main wheel is centrally located and engaged on the central shaft, the second two wheels are engaged on the two side shafts as shown in the Figure 3.1 (a).

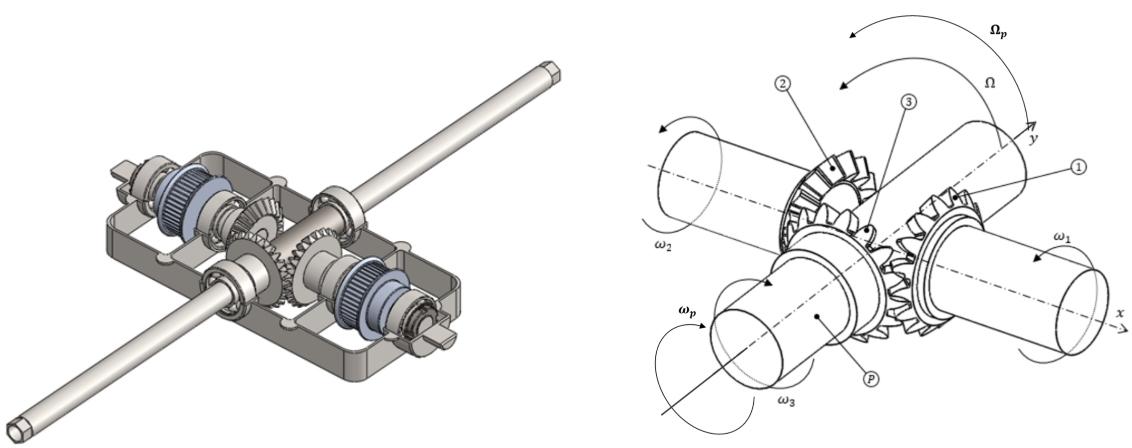

(a) Differential system (b) Considered rotational speeds

Figure 3.1: Representation of the differential system

The central shaft is connected to the spherical shell, while the side shafts are connected to the motors through the implementation of pulleys and belts. The working principle of the differential system has been derived and formalised through the following formulas:

$$\omega_3 + \omega_p = \frac{\omega_1 - \omega_2}{2} \tag{3.1}$$

$$\Omega + \Omega_p = \frac{\omega_1 + \omega_2}{2} \tag{3.2}$$

Where:

- ω_3 and Ω are respectively the forward and tilting speed of the sphere
- ω_p and Ω_p are the forward and tilting speed of the pendulum
- ω_1 and ω_2 are the rotational speed of the lateral shafts

The positive directions are defined in the scheme of Figure 3.1 (b).
The rover was then completed with the developement that houses the motors. This choice lowers the system Center of Mass (COM), which brings a higher ability to overcome obstacles and climbing slopes.
The final system presents a pendulum able to change both forward and lateral angel. In forward rotation, the differential box follows the motion of the pendulum. In lateral rotation, pendulum present a degree of freedom respect to the differential box. The shell was developed as a series of steel bands that converge to the central shaft terminals. Finally, a shell is mounted on the steel strips. The material of the external layer of the shell must be chosed depending on the application.
The final prototype is reported in the following figure:

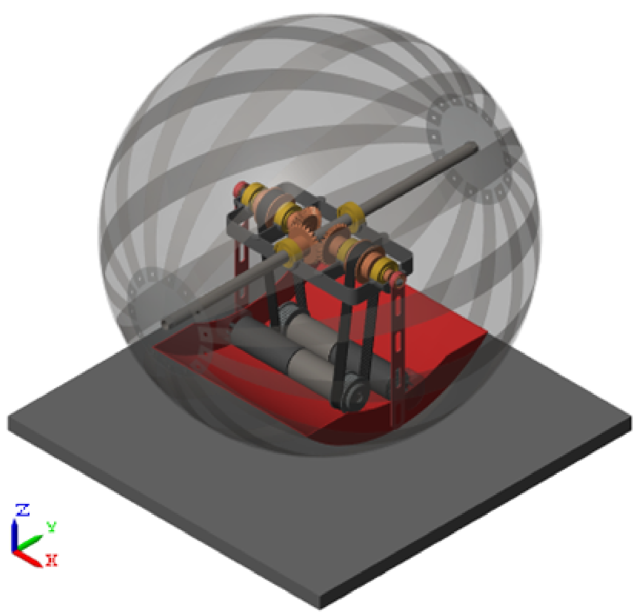

Figure 3.2: Prototype of M. Melchiorre SR

The work proceeded with the development of a control strategy. Three approaches were defined in order to derive and validate a controller for the plant.
Firstly, a overall multibody of the prototype has been imported in Simulink/Simscape environment. Although the model presented several oscillation when reaching the set values, the performance revealed high controllability in both linear and curved trajectories. Results can be seen in Figures 3.3:

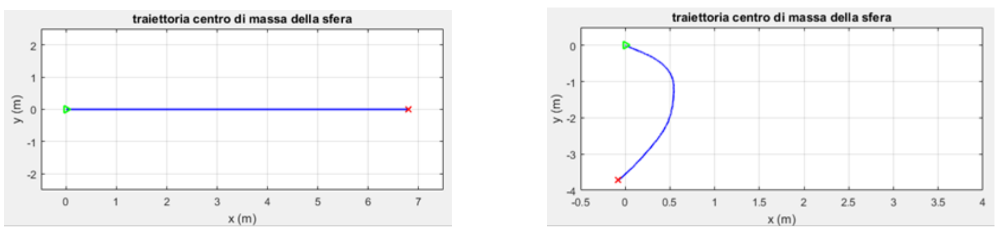

COM straight trajectory

COM curve trajectory

Figure 3.3: Graphics representing the system behaviour.

To derive a more precise controller, differential equations of the spherical shell were derived by means of Euler-Lagrange. Although the internal mechanics were not modelled, the final result is a set of equations that describes the sphere dynamic when subject to torque applied in Roll and Yaw directions. The equations considered the non-holonomic constraints that define the movement of a sphere on a plane. By defining the torque applied on the sphere, it is possible to derive the position and speed profile of the system. The torque that actuate the sphere can be found as the torque acting between the central shaft and the pendulum.

Finally, a simple multibody model was implemented. The model presented same masses and COM position of the prototype. Actuation is provided as torque applied directly at pendulum junction with the differential box. Thus, this model allowed to impose torques that were defined as inputs variables of the analytical model.
In in Figure 3.4 it is possible to see the comparison between the simplified model and the analytical one when the inputted torque are the same.

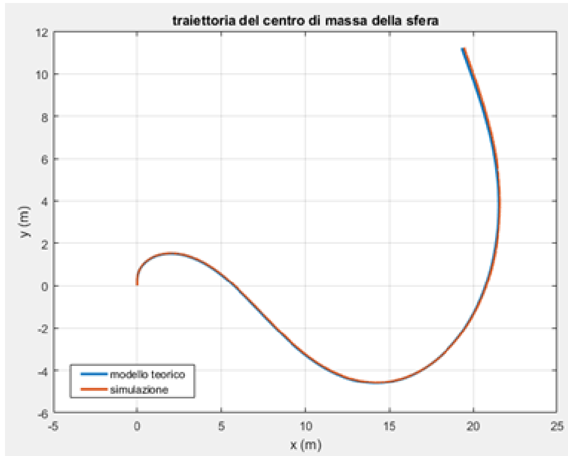

Figure 3.4: Comparison between Analitycal and Multibody model.

3.2 Colamartino's Thesis

The work developed by T. Colamartino [2] had as primary objective the enhancement of the provided torque for obstacle overcoming. The resulting improvement consisted in the implementation of two CMG groups above the precedent design.
Based on the physical principle of the conservation of the angular momentum, the activation of the gyroscopic maneuver consents an increment of the maximum climbing step. Gyroscopic torque is generated by imposing a spinning rotation ω to a flywheel with inertia I_{fl} and - simultaneously - imposing a titling speed Ω over a perpendicular direction of the spinning rotation. The relation between the maximum step and the gyroscopic torque has been derived as follows:

$$\begin{cases} \tau_G = 2 \cdot I_{fl}\, \omega\, \Omega \\ \dfrac{h}{R} = 1 - \sqrt{1 - \left(\dfrac{a + \frac{\tau_G}{(m_p + M_s)\, g}}{R} \right)^2} \end{cases} \tag{3.3}$$

After several computations, CMGs were finely dimensioned. The spinning and tilting velocity were defined a flywheel design has been developed in order to obtain a value of I_{fl}. Viscous forces were accounted and their effect was limited by providing an external shell to the rotating flywheels. Motors of both main actuation and of the gyroscopic system actuation were selected in order to satisfy the requirements of minimum $10cm$ step h and a $25cm$ radius R. The new structure of the pendulum is presented in Figure 3.5:

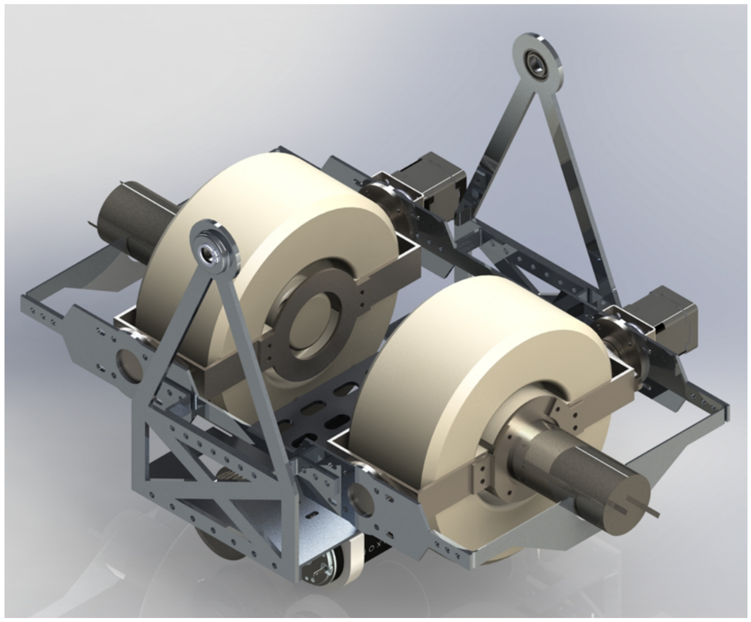

Figure 3.5: Pendulum design

A 2D dynamic study was performed through Lagrange formulation to obtain the analytical equations of the forward motion. The analytical model is later compared to the multibody model created in Simulink/Simscape to evaluate the performances of the robot and the reliability of the two approaches. Finally, the last part of the thesis focuses on the controller design. The controller developed is a Fuzzy PID, meaning the parameters K_p, K_i, K_d are actively set by a Fuzzy algorithm.

3.3 Thesis contribution

The work starts from the inherited rover and presents the advances in design and control, with a view to the final prototype. Overall, the work is divided into two parts: the fist part in on the design and aims to derive a version of the robot suitable for prototyping; the second part is on multibody modelling and control, and aims to design a control scheme suitable for curved trajectories. In particular, this thesis describes the first part of the work, and reports on the study of the selection of

electronic components and on the structural design of the locomotion mechanism.
The electronic components are selected depending on the required function for the actuation of a control strategy. Encoders are needed to derive the speed and the position of the motors, while IMU sensor must be implemented to acquire position and speed information of the overhall system. Drivers are essential for imposing a set value to motors. A transceiver is needed to acquire signals imposed through external controller. Finally, a microcontroller is necessary to acquire, elaborate and generate a control actuation for the system. It is important to select the components in order to satisfy the desired continuous operating range. Continuous and peak current of every component must verified to properly operate in the various working points of the rover. The MCU must have sufficient numbers of pin and computational power for control actation. Finally, since the pendulum is constantly rotating respect to the shell, it must be provided a position of the electronics that does not limits the rotation.
The mechanical components of the structure must be properly sized in order to bear the forces and torques deriving form the pendulum inclination. In order to meet h and R objectives, the corresponding maximum torque can be elaborated using the formula 3.3. The design has to be as symmetric as possible, in order to not misalign the system's COM position. Finally, the order of the feasibility of the assembly needs to considered.

In part two, a new multibody model is realized in order to analyze the final design. Several tests are carried out to measure the rover's performance. A control strategy to operate curved trajectories was derived. Control via external joypad has been implemented too. Performance under different plane conditions were determined.

Chapter 4

Design review

4.1 Introduction

In the following chapter, the work carried out to develop a buildable prototype is presented. The starting point was the robot discussed in Colamartino's thesis [2]. This chapter meticulously reviews every aspect of the electronic system and mechanical components. Where necessary, revisions were made to refine or optimize the previous design.
The first part focuses on the electronics, describing the various implemented components and their placement within the rover's structure. In the second part, the mechanical components are examined, with particular attention to the sizing of the supporting structure under maximum load conditions. In the end, the final design of the robot is presented including the estimated production costs.

4.2 Electronics

A significant part of the project accounts for the electronic design.
Starting point for the development of the electronic system are the motors. There are two DC motors for the movement of the pendulum and the sphere, and four motors – two spinning motors and two stepper motors – for managing the gyroscopic system. Motor had already been selected, but further analysis to verify their suitability for the required purpose were made.

Electronics choice was totally elaborated in this thesis. Drivers were chosen according to the operating conditions of the rover, while sensors and encoders were selected for the actuation of a control strategy.
The following paragraphs present the choices made and conclude with a schematic of the electronics connection.

4.2.1 Pendulum main motors and planetary gearheads

These are the main motors of the system; through their actuation it is possible to vary the inclination of the pendulum and transmit motion to the sphere. As indicated by previous works [2], the motors identified as suitable are the **Maxon RE 40** [33] with a nominal voltage of $24V$.

RE 40 ∅40 mm, graphite brushes, 150 watt

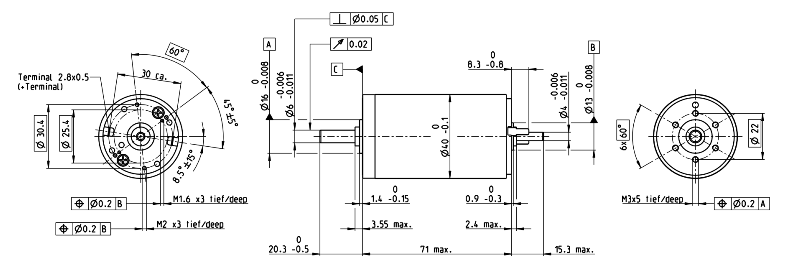

Stock program
Standard program
Special program (on request)

Motor Data		Part Numbers: 148866	148867	148877	218008	218009	218010	218011	218012	218013	218014
Values at nominal voltage											
1 Nominal voltage	V	12	24	48	48	48	48	48	48	48	48
2 No load speed	rpm	6920	7580	7590	6420	5560	3330	2690	2130	1720	1420
3 No load current	mA	241	137	68.6	53.7	43.7	21.9	16.6	12.5	9.66	7.76
4 Nominal speed	rpm	6380	6940	7000	5810	4930	2710	2060	1510	1080	781
5 Nominal torque	mNm	94.9	177	187	186	180	189	190	192	192	190
6 Nominal current (max. continuous current)	A	6	6	3.17	2.66	2.23	1.4	1.13	0.909	0.73	0.6
7 Stall torque	mNm	1720	2420	2560	2040	1620	1020	814	655	523	424
8 Stall current	A	105	80.2	42.4	28.6	19.7	7.43	4.79	3.06	1.97	1.32
9 Max. efficiency	%	88	91	92	91	91	89	89	88	86	85
Characteristics											
10 Terminal resistance	Ω	0.115	0.299	1.13	1.68	2.44	6.46	10	15.7	24.4	36.3
11 Terminal inductance	mH	0.024	0.082	0.33	0.46	0.613	1.7	2.62	4.14	6.41	9.32
12 Torque constant	mNm/A	16.4	30.2	60.3	71.3	82.2	137	170	214	266	321
13 Speed constant	rpm/V	581	317	158	134	116	69.7	56.2	44.7	35.9	29.8
14 Speed/torque gradient	rpm/mNm	4.05	3.14	2.97	3.16	3.45	3.29	3.31	3.27	3.29	3.37
15 Mechanical time constant	ms	5.89	4.67	4.28	4.2	4.19	4.16	4.15	4.15	4.15	4.16
16 Rotor inertia	gcm^2	139	142	137	127	116	121	120	121	120	118

Figure 4.1: Maxon RE 40 technical data.

To obtain the required values of rotational speed and torque for the actuation, the **Planetary Gearbox GP 42 C** [34] have been selected.

Planetary Gearhead GP 42 C ∅42 mm, 3.0–15.0 Nm
Ceramic Version

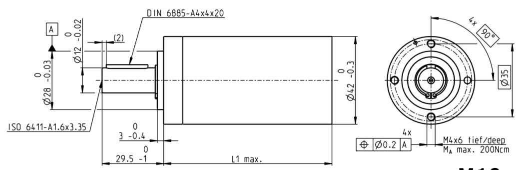

M 1:2

Technical Data		
Planetary Gearhead		straight teeth
Output shaft		stainless steel
Bearing at output		preloaded ball bearings
Radial play, 12 mm from flange		max. 0.06 mm
Axial play at axial load	< 5 N	0 mm
	> 5 N	max. 0.3 mm
Max. axial load (dynamic)		150 N
Max. force for press fits		300 N
Direction of rotation, drive to output		=
Max. continuous input speed		8000 rpm
Recommended temperature range		-40...+100°C
Number of stages		1 2 3 4
Max. radial load, 12 mm from flange		120 N 240 N 360 N 360 N

Stock program
Standard program
Special program (on request)

		Part Numbers									
		203113	203115	203119	203120	203124	203129	203128	203133	203137	203141
Gearhead Data											
1 Reduction		3.5:1	12:1	26:1	43:1	81:1	156:1	150:1	285:1	441:1	756:1
2 Absolute reduction		7/2	49/4	26	343/8	2197/27	156	2401/16	15379/54	441	756
10 Mass inertia	gcm²	14	15	9.1	15	9.4	9.1	15	15	14	14
3 Max. motor shaft diameter	mm	10	10	8	10	8	8	10	10	10	10
Part Numbers		203114	203116	260552*	203121	203125	260553*	203130	203134	203138	203142
1 Reduction		4.3:1	15:1	36:1	53:1	91:1	216:1	186:1	319:1	488:1	936:1
2 Absolute reduction		13/3	91/6	36/1	637/12	91	216/1	4459/24	637/2	4394/9	936
10 Mass inertia	gcm²	9.1	15	5.0	15	15	5.0	15	15	9.4	9.1
3 Max. motor shaft diameter	mm	8	10	4	10	10	4	10	10	8	8
Part Numbers		260551*	203117		203122	203126		203131	203135	203139	260554*
1 Reduction		6:1	19:1		66:1	113:1		230:1	353:1	546:1	1296:1
2 Absolute reduction		6/1	169/9		1183/18	338/3		8281/36	28561/81	546	1296/1
10 Mass inertia	gcm²	4.9	9.4		15	9.4		15	9.4	14	5.0
3 Max. motor shaft diameter	mm	4	8		10	8		10	8	10	4
Part Numbers			203118		203123	203127		203132	203136	203140	
1 Reduction			21:1		74:1	126:1		257:1	394:1	676:1	
2 Absolute reduction			21		147/2	126		1029/4	1183/3	676	
10 Mass inertia	gcm²		14		15	14		15	15	9.1	
3 Max. motor shaft diameter	mm		10		10	10		10	10	8	
4 Number of stages		1	2	2	3	3	3	4	4	4	4
5 Max. continuous torque	Nm	3.0	7.5	7.5	15.0	15.0	15.0	15.0	15.0	15.0	15.0
6 Max. intermittent torque at gear output	Nm	4.5	11.3	11.3	22.5	22.5	22.5	22.5	22.5	22.5	22.5
7 Max. efficiency	%	90	81	81	72	72	72	64	64	64	64
8 Weight	g	260	360	360	460	460	460	560	560	560	560
9 Average backlash no load	°	0.6	0.8	0.8	1.0	1.0	1.0	1.0	1.0	1.0	1.0
11 Gearhead length L1**	mm	41.0	55.5	55.5	70.0	70.0	70.0	84.5	84.5	84.5	84.5

*no combination with EC 45 (150/250 W) and EC-i 40
**for EC 45 flat L1 is -3.6 mm

Figure 4.2: Maxon Planetary Gearhead GP 42 C technical data.

The design goal is climbing a slope of 15° at a speed of $2.5m/s$ as nominal operating point. These characteristics are met imposing as continuous working point $7735rpm$ and $134.25mNm$ for each motor. After a meticulous comparison of different set-ups, this combination has been selected as best trade-off for dimensions and operational capacity. A detailed analysis of the examined load conditions is provided in the Part 2 of the work of thesis.

In accordance with previous designs, motors have been placed at the bottom of the pendulum to maintain the system's COM as close to the ground as possible. A pair of belts allow torque and rotational speed transmission the differential gearbox located at the center of the SR. From here, motion is transmitted to the sphere through bevel gears.

DC motors are controlled imposing the injected current and the supply voltage, the imposition of a working condition is actuated through devices called drivers. The connection between these motors and the drivers is obtained through two wires – M^+ and M^- – that represent the positive and negative terminal of the motors.

4.2.2 Drivers of the pendulum main motors

A driver is an electronic device capable of controlling the power supply and the working point of the DC motor to which it is connected. It acts as an intermediary between the MicroController Unit (MCU) and the motor, modulating the current and voltage supplied to manage the speed and direction of the rotor's rotation.
The main considerations for choosing a driver include the nominal current, peak current, and motor protection systems. These devices play a crucial role in the robot's operation, as they must be reliable in managing the motion of the system and safeguarding actuators from potential damage.
ESCON 50/5 [35] were finally selected as drivers.

Figure 4.3: Maxon ESCON 50/5.

Important characteristics about this driver are:

- Nominal operating voltage: $10 - 50\ V_{DC}$
- Maximum continuous current: $5A$
- Peak current: $15A$
- Operating mode: current controller (torque control), position controller, speed controller (closed and open loop)
- Overvoltage and undervoltage protection

- Overcurrent protection
- Thermal overload protection

An additional advantage of this choice was the compatibility and optimization ensured by Maxon when pairing products they have designed.

As can be seen in Figure 4.3, pin schematic of the driver is divided in different sections. In section J1 of the driver pins it is possible to attach the power supply of the controlled motor. In section J2 are the motor connections M^+ and M^-. If the motor is using a Maxon encoder, J4 connection can be used to acquire data. Sections J5 and J6 are respectively input/output digital pins and input/output analog pins. These pins can be configured basing on which information the user wants to acquire. Connection between MCU and a single driver requires at least two analog output to measure motor speed and current. This information is important to implement a control strategy and to know the power consumption of the motors.

4.2.3 Encoders of pendulum main motors

An encoder is a device that acquires feedback data about the position, speed and rotational direction of DC motors. Their implementation is fundamental for a precise control of the motors.
The chosen encoders are the **HEDL 5540** [36].

Part Numbers	110512	110514	110516	110518	X drives
Type					
Counts per turn	500	500	500	500	500
Number of channels	3	3	3	3	3
Max. operating frequency (kHz)	100	100	100	100	100
Max. speed (rpm)	12000	12000	12000	12000	12000
Shaft diameter (mm)	3	4	6	8	2–4

Figure 4.4: Maxon HEDL 5540 technical data.

They are incremental encoders, this means the generated electrical impulses are proportional to the shaft movement. The acquisition is taken directly form the posterior shaft of the motor; assemblage is operated by Maxon itself. These encoders have a resolution of 500 pulses per revolution and they are equipped with 3 output channels. Two differential signal channels A and B, which allow determining the direction of rotation and counting the number of pulses, and an index channel.
The connection between the encoders and the selected drivers is performed through a specific connector.

4.2.4 Spinning motors of CMG

These are motors designed to spin the flywheels at constant speed along their symmetry axis. The speed generated by these motors is the spinning speed ω that, combined with the tilting speed Ω, generates the gyroscopic moment τ_G. As reported in [2], the generated torque for a single CMG group is:

$$\vec{\tau_G} = I_{fl}\,\vec{\omega} \wedge \vec{\Omega} \tag{4.1}$$

where I_{fl} is the flywheel inertia along the spinning axis.

It is important that these motors can reliably reach and maintain a minimum speed for the correct implementation of the gyroscopic moment and – simultaneously – they should deliver enough torque to support the inertia of the flywheel and the air friction. All the consideration about the sizing of the motors were elaborated in [2], the final choices were two brushed motors **Maxon DCX 35 L** [37] with $12V$ as nominal voltage.

The speed profile required by these motors is the same for every application. Their task is to reach a speed and maintain it steadily for a duration of 1 second to perform the gyroscopic maneuver. An open-loop control approach has been deemed sufficient; therefore no encoders are planned to be paired with the motors.
The connection between a motor and its driver is performed through two wires: M^+ and M^-.

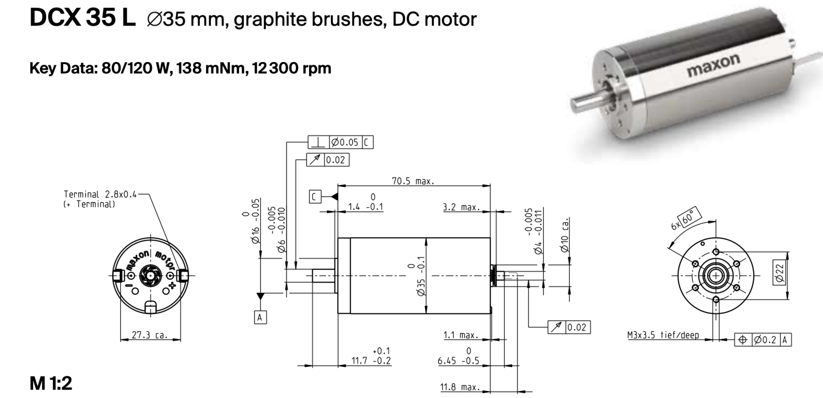

Motor Data								
1_	Nominal voltage	V	12	18	24	36	48	60
2_	No load speed	rpm	8130	7200	7720	7940	6670	7690
3_	No load current	mA	320	177	146	101	58.6	57.5
4_	Nominal speed	rpm	7610	6640	7160	7410	6140	7160
5_	Nominal torque	mNm	77.7	120	121	128	138	132
6_	Nominal current (max. continuous current)	A	6.00	5.32	4.26	3.07	2.08	1.84
7_	Stall torque	mNm	2080	1980	2030	2160	1860	2050
8_	Stall current	A	152	84.8	69.3	50.3	27.3	27.7
9_	Max. efficiency	%	85	88	89	90	90	90
10_	Terminal resistance	Ω	0.079	0.212	0.346	0.716	1.76	2.16
11_	Terminal inductance	mH	0.026	0.077	0.121	0.260	0.658	0.776
12_	Torque constant	mNm/A	13.7	23.4	29.3	42.9	68.3	74.1
13_	Speed constant	rpm/V	699	408	326	223	140	129
14_	Speed/torque gradient	rpm/mNm	4.04	3.70	3.86	3.72	3.61	3.76

Figure 4.5: Maxon DCX 35 L technical data.

4.2.5 Drivers of spinning motors

Since this application does not require the same responsiveness of the pendulum motors, a different driver can be chosen. To achieve a good compromise between control reliability, dimensions and cost, H-bridge drivers **BTS7960** [38] have been selected.

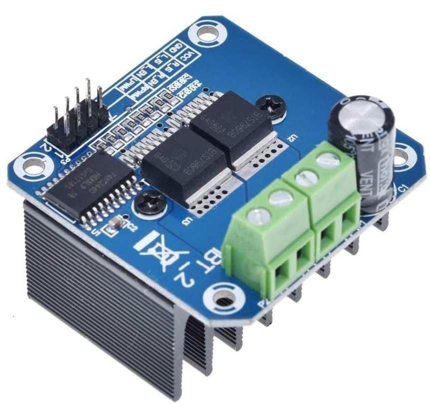

Figure 4.6: Driver BTS7960.

Brief data about this driver are:

- Nominal operating voltage: 6 – 27 V_{DC}

- Peak current: $43A$
- Current limitation
- Overvoltage lock out
- Undervoltage shut down
- Overtemperature protection
- Short circuit protection

As input pins there are B^+ and B^-, respectively positive and negative motor power supply. As output pins there are M^+ and M^- and must be attached to motors terminal. Their activation determines the positive or negative rotation of the motor.
Figure 4.7 shows the control input pin functions of the driver.

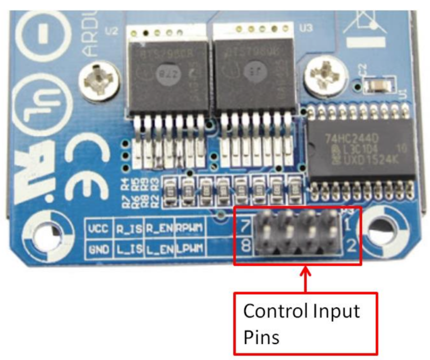

Pin No	Function	Description
1	RPWM	Forward Level or PWM signal, Active High
2	LPWM	Reverse Level or PWM signal, Active High
3	R_EN	Forward Drive Enable Input, Active High/ Low Disable
4	L_EN	Reverse Drive Enable Input, Active High/Low Disable
5	R_IS	Forward Drive, Side current alarm output
6	L_IS	Reverse Drive, Side current alarm output
7	Vcc	+5V Power Supply microcontroller
8	Gnd	Ground Power Supply microcontroller

Figure 4.7: Driver BTS7960 pin connection and function.

R_{IS} and L_{IS} are the only analog pins, a microcontroller requires at least two analog input pins to read their signals. Direction and speed of the motor are imposed using EPWM, LPWM, R_{EN} and L_{EN} pins. BTS7960 driver can operate with PWM frequencies up to $25kHz$.

4.2.6 Tilting motors of CMG

"Tilting" refers to the action by which gyroscopic groups are rotated of 90° at a constant speed Ω while the spinning motors are in action. Moreover, these motors are used to position the gyroscopes inside the pendulum structure.
The characteristics that these motors must meet are the rotational speed of the maneuver and the torque to be delivered. Stepper motors have been chosen for this function as they offer an adequate compromise for the required size and operating point.

The dynamics of the CMG maneuver have already been addressed by [2] and a final speed of $15rpm$ has been imposed. Torque sizing must be computed to overcome the resisting torque of CMG group. Torque balance along stepper motor main axis is:

$$\tau_M = I_{CMG}\,\alpha + m_{CMG}\,d\,g\,sin(\theta) \tag{4.2}$$

Where:

- I_{CMG} is the CMG group inertia
- α is the axial acceleration of the CMG group
- m_{CMG} is the global mass of the CMG group
- d is the distance between the rotation axis and the CMG center of mass
- θ is the angle between d and the effective component of the gravity force
- τ_M is the torque required at the motor shaft

Since costant speed is imposed, α is set to zero. Worst case scenario must be considered to compute maximum needed torque. Imposing $\theta = 90°$, the relation becomes:

$$\tau_M = m_{CMG}\,d\,g \tag{4.3}$$

Since CMG have already been modelled in precedent works, measures of m_{CMG} and d can be derived by correspondent SolidWorks (SW) files.

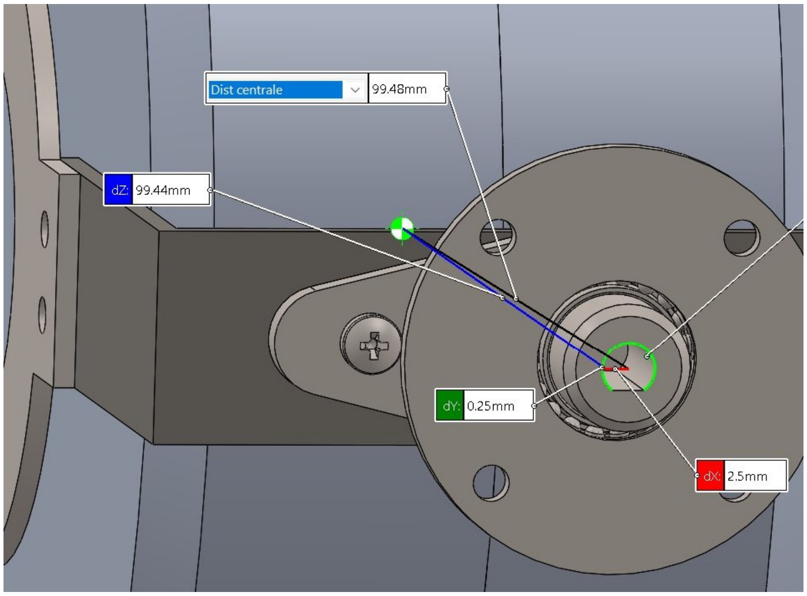

Figure 4.8: Distance between rotational axis and CMG center of mass.

Motor efficiency, frictional torques and a safety coefficient must be accounted. The final maximum torque value needed from the motor is:

$$\tau_{M_{eff}} = CS \, \frac{\tau_M}{\eta_M \, \eta_F} \tag{4.4}$$

The starting values and the final result are listed in Table 4.1:

Table 4.1: Data and results for stepper torque computation.

DATA AND RESULTS		
m_{CMG}	$5.44kg$	Mass of a CMG group
d	$0.25cm$	Distance between barycenter and axis
CS	2	Safety coefficient
η_M	0.80	Efficiency of the motor
η_F	0.90	Coefficient of the frictional forces
$\tau_{M_{eff}}$	$37.1Ncm$	Torque required at the motor

Since the previously selected stepper motor, the QSH2818, was unable to deliver the computed torque, a different motor was sought. Finally, the motor that satisfies both speed and toque characteristics is **Nema 17** [39] with an holding torque of $40Ncm$.

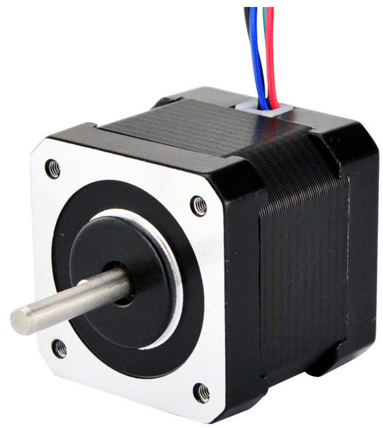

Figure 4.9: Motor Nema 17.

Another situation to consider is the static condition. Torque due to gravity acts constantly, and its presence must be accounted to avoid undesired movements of CMG groups. Indeed, it is necessary that the CMGs remain stationary when not engaged in generating τ_G. The datasheet does not report the detent torque for Nema 17 motor, defined as the torque generated by a stepper motor when it is not powered. Its value may not be sufficient to compensate for the torque resulting from the gravitational force. An initial hypothesis to keep the assembly stationary was to integrate a brake into the motor, however this solution was abandoned due to insufficient space. The only remaining choice was to keep the stepper motors constantly energized.
The search for a motor that could be the best compromise between the required operating points and power consumption reconfirmed the Nema 17 as final choice.

Table 4.2: Data of Nema 17.

DATA	
Nominal current	$0.4A$
Holding torque	$40Ncm$
Step Angle	$1.8°$
4 connection wires	A^+ and A^- (first winding) B^+ and B^- (second winding)

Injected voltage depends on driver, and it may vary depending on the configuration. The important parameter to control stepper motors is the injected current.

4.2.7 Drivers of tilting motors

The **TMC2208** [40] driver boards were chosen to control the stepper motors. These devices are widely used components in applications requiring precise and silent control of stepper motors. They include the microstepping functionality, allowing a smooth and precise motor control.

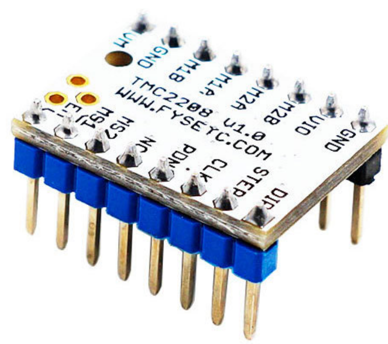

Figure 4.10: Driver TMC2208.

TMC2208 main characteristics are:

- Maximum continuous current: $1.4A$
- Peak current: $2.0A$
- Voltage range: $4.75 - 36V$
- Up to 256 native microsteps (without interpolation)

TMC2208 uses digital pins only. Pins to control the motors are M1A and M1B for the first winding, M2A and M2B for the second winding. Pins VM and GND are necessary to power supply the motor. STEP, DIR, EN are necessary to control movement, direction and activation of the motor. MS1 and MS2 are implemented when using microstepping. PDN can be used for UART communication if desired or to control standstill current.

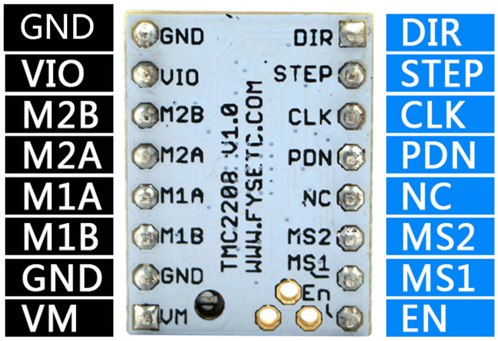

Figure 4.11: TMC2208 pin schematic.

Table 4.3: TMC2208 pin functions.

PIN	FUNCTION
GND	Ground
VM	Motor Supply Voltage
VIO	Logic Supply Voltage
M1A	Motor Coil 1
M1B	Motor Coil 1
M2A	Motor Coil 2
M2B	Motor Coil 2
STEP	Step-Signal Input
DIR	Direction-Signal Input
EN	Enable Motor Outputs: GND=on, VIO=off
MS1	Step-Configuration
MS2	Step-Configuration
PDN	UART and Auto Power Down Control: GND=on, VIO=off
CLK	Clock Input
DIAG	Diagnostics Output
INDEX	Index Output
VREF	Analog Reference Voltage
NC	Not Connected

4.2.8 Encoder of tilting motors

The encoders to control the tilting motors are the **AS5600** [41].

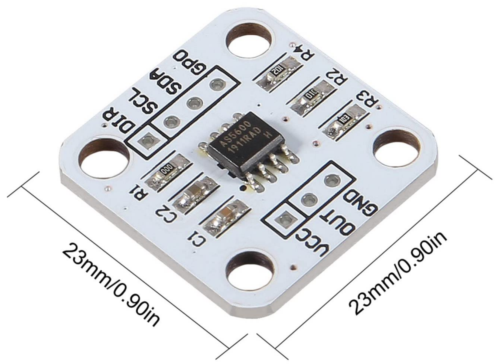

Figure 4.12: Encoder AS5600.

These encoders have a magnetic rotary position sensor. Important aspects of these components are the high resolution and precision, low power consumption, wide temperature range.

Table 4.4: Pin description of the encoder AS5600.

PIN	FUNCTION	DESCRIPTION
VCC	Supply	Positive voltage supply in 3.3V mode (requires an external 1-µF decoupling capacitor in 5V mode)
OUT	Analog/digital output	Analog/PWM output
GND	Supply	Ground
PGO	Digital input	Program option (internal pull-up, connected to GND = Programming Option B)
SDA	Digital input/output	I^2C Data (consider external pull-up)
SCL	Digital input	I^2C Clock (consider external pull-up)
DIR	Digital input	Direction polarity (GND = values increase clockwise, VDD = values increase counterclockwise)

The connection to microcontroller must include the SLC and SDA pins. Their function is to transmit motor rotation angle information via the I^2C protocol. The DIR digital pin is employed to set the positive direction of rotation. These components must be placed behind the stepper motors.

4.2.9 IMU sensors

IMU sensors are components able to measure motion, orientation and gravitational forces through accelerometers and gyroscopes.

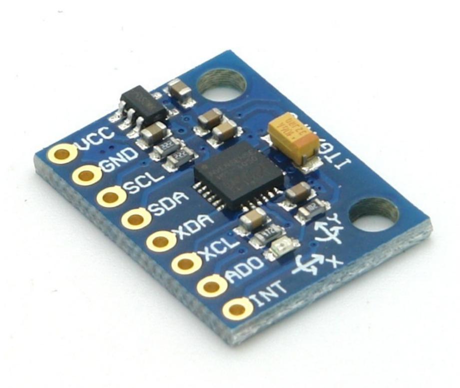

Figure 4.13: IMU sensor MPU-6050.

Two **MPU-6050** [42] sensors were selected to acquire position, angles, linear and rotational speed, and linear and rotational acceleration of sphere and pendulum. These devices use the I^2C communication and have the following range:

- Gyroscope: ± 250, 500, 1000 and $2000°/s$
- Accelerometer: +2, +4, +8, $+16g$

The first IMU is placed under the lower case of the differential box, and it can compute the position of the sphere barycenter, the forward inclination of the pendulum and all the motion derivatives of these quantities.
The second IMU is placed on the pendulum structure, and it is used to acquire the lateral angle inclination and all the relative derivatives.

Table 4.5: Pin description of the IMU MPU-6050.

PIN	NAME	DESCRIPTION
VCC	Supply	Provides power for the module, can be $+3V$ to $+5V$. Typically $+5V$ is used.
GND	Ground	Connected to Ground of system.
SCL	Serial Clock	Used for providing clock pulse for I^2C Communication
SDA	Serial Data	Used for transferring Data through I^2C communication.
XDA	Auxiliary Serial Data	Can be used to interface other I^2C modules with MPU6050. It is optional.
XCL	Auxiliary Serial Clock	Can be used to interface other I^2C modules with MPU6050. It is optional.
ADO	Address	If more than one MPU6050 is used a single MCU, then this pin can be used to vary the address.
INT	Interrupt	Interrupt pin to indicate that data is available for MCU to read.

SCL and SDA pins are used to send information to microcontroller using I^2C communication. AD0 pin is enabled when using multiple IMUs identify data address. INT pin is used to notify to MCU that new measures are available from MPU-6050.

4.2.10 Bore slip rings

A need that arose during the construction of the rover was to be able to recharge the batteries without disassemble the shell.
The path of the wires designated for charging the batteries should start from batteries, positioned on the pendulum, and proceed along the main shaft until exiting through the side holes. The issue with this configuration is that the pendulum and the main shaft are in a state of relative rotation when the robot moves forward. Consequently, cables running directly from the batteries to the side holes would twist around the main shaft and eventually break. Therefore, a component capable of decoupling the

rotational motion between the shaft and pendulum was sought. After some research, the choice fell on Bore Slip Rings.

Bore slip rings are electromechanical components used to transmit electrical signals and power from a stationary part to a rotating part of a system. They are particularly useful in applications where continuous electrical contact between rotating and fixed parts is necessary without restricting rotary motion. They are through-hole components; therefore, they can be mounted on the main shaft of the rover.
The identified components are the **H-1532 series** [43] of Sering company:

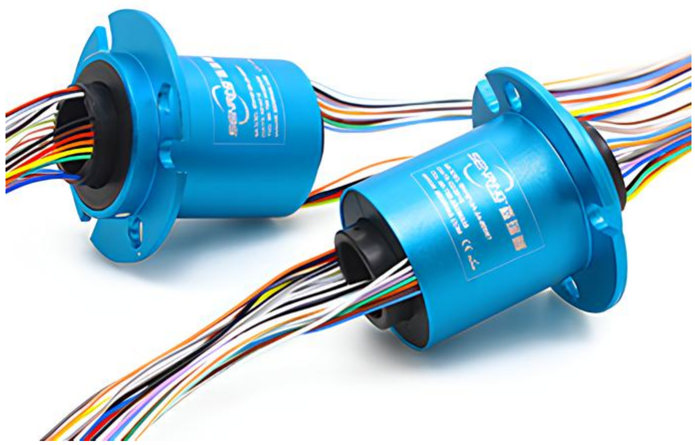

Figure 4.14: Bore slip rings of H-1532 series.

Key information are reported in Table 4.6.

Table 4.6: Data of H-1532 series.

DATA	
Inner diameter	$15mm$
Outer diameter	$32.8mm$
Length	$41.7mm$
Max rotating speed	$250rpm$, $600rpm$, $1000rpm$
Circuits number	6, 12, 18, 24
Circuit function	Signals or $0-2A$

Circuits can be combined in parallel for bigger current, N circuits of $2A$ to get $N \cdot 2A$.

Number of wires must be chosen depending on the required charging speed. Supposing $10A$ as maximum charge current, H1532-06S can be a valid choice.
Two bore slip rings would be mounted on the main shaft of the rover, to have faster battery charge and to allow signal communication with MCU if needed. Also, this choice maintains a symmetric design.

4.2.11 Transmitter

One of the objectives of the final rover is to enable its navigation to be controlled via an external controller. To achieve this, it is necessary to define an antenna capable of capturing incoming signals and then having them processed by the microcontroller.
The transceiver **NRF24L01** [44] was selected as the optimal choice due to its versatility, the comprehensive online documentation, and its transmission characteristics.

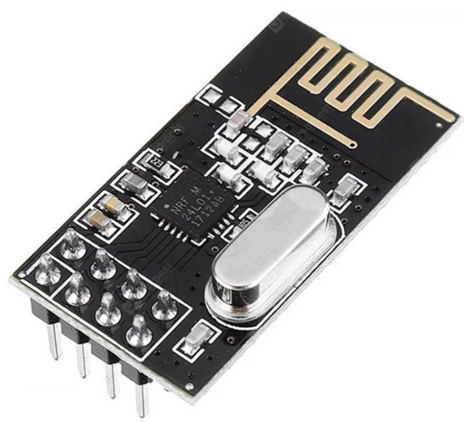

Figure 4.15: Transceiver NRF24L01.

Main aspects regarding this device are:

- Operates in the $2.4GHz$ ISM (Industrial, Scientific and Medical) band
- Effective communication range up to $100m$
- Baud rate: $250kbps$, $1Mbps$, and $2Mbps$
- Power supply range: $1.9 - 3.6V$
- 125 RF channels supported

- Maximum operating current: $250mA$
- Maximum pipelines: 6

The pins are reported in Table 4.7.

Table 4.7: Pin description of the NRF24L01.

PIN	**NAME**	**DESCRIPTION**
VCC	Supply	Powers the module using $3.3V$
GND	Ground	Connected to the Ground of the system
CE	Chip Enable	Used to enable SPI communication
CSN	Chip Select Not	This pin has to be kept high always, else it will disable the SPI
SCK	Serial Clock	Provides the clock pulse using which the SPI communication works
MOSI	Master Out Slave In	Connected to MOSI pin of MCU, for the module to receive data from the MCU
MISO	Master In Slave Out	Connected to MISO pin of MCU, for the module to send data from the MCU
IRQ	Interrupt	It is an active low pin and is used only if interrupt is required.

Connections with the microcontroller unit do not require analog pins. The communication protocol of the NRF24L01 uses the Serial Peripheral Interface (SPI) interface. Transmission and reception are operated through radio frequency modulation. All pins must be connected to the microcontroller, except for IRQ which can be left floating.

To increase the power and the range of the transmission, a NRF24L01+PA+LNA can be chosen instead. A disadvantage of this choice would be higher power consumption and thus shorter battery life. Pins and communication protocols are the same of the NRF24L01.

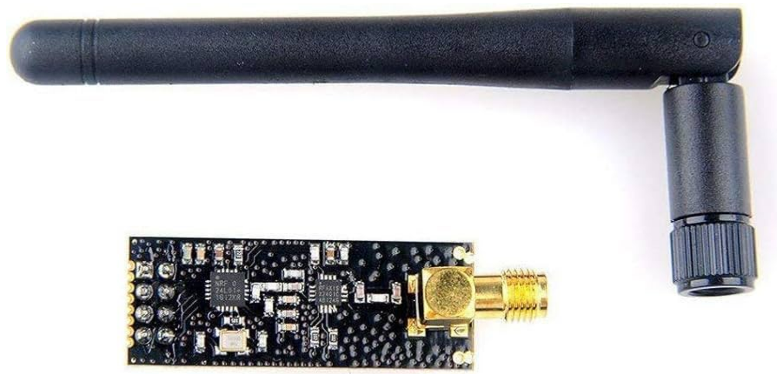

Figure 4.16: Transceiver NRF24L01+PA+LNA.

4.2.12 Controller

A simple joypad can be developed for controlling the rover. The requirements that the joypad must meet are the following:

- Regulation of forward velocity of the sphere
- Regulation of tilting velocity of the sphere
- Activation of the gyroscopic manoeuvre

It is possible to follow several online tutorials which provide guidance on the construction of such a system. Modelling a controller requires:

- NRF24L01 or upgrades
- Arduino Nano
- Two 2-axis joystick
- One push-button
- Power source
- PCB board
- Wires, header and capacitors for connections

Code is used to assign actions and intensities to be performed by components. The example in Figure 4.17 from [45] uses the aforementioned components in a controller. This controller can serve as a reference for implementing more complex commands.

Figure 4.17: Joypad example.

4.2.13 Microcontroller

The purpose of the components mentioned so far is to measure the internal states of the robot and to actuate motion. The data that is collected by the sensors must be processed in order to derive the position and speed of the rover, and must also be implemented in a control strategy capable of managing the movement of the system. The component assigned to this task is the microcontroller.

A microcontroller is an integrated circuit that is capable of governing specific functions within embedded electronic systems. Also known as the MCU, these components comprise a single integrated circuit that incorporates a Central Processing Unit (CPU), a Random-Access Memory (RAM) for temporary data processing, a Read-Only Memory (ROM) for storing the executable program, and several input/output (I/O) pins for interfacing with external devices. When selecting a microcontroller, it is essential to consider several key factors, including the number of pins, the complexity of the programming process, the computing power and the cost.

The term “control strategy” refers to an algorithm that enables the regulation of the rover’s behaviour. It is essential that the control strategy is capable of regulating the robot’s forward and tilting motion by imposing specific speed values on the pendulum

motors. Furthermore, the control strategy must be capable of regulating the speeds of the tilting and spinning motors to execute the gyroscopic manoeuvre. Particular attention has to be paid to the stepper motors on which a reference angle is imposed constantly to hold the CMG in position.
In conclusion, the control strategy imposes the following values: the speed of the Maxon RE 40 motors, the speed of the DCX 35 L motors, and the speed and position of the Nema 17 motors.

The number of connections provided between the microcontroller and the rest of the electronics is summarized in Table 4.8.

Table 4.8: Total pin required from the microcontroller.

COMPONENTS	**A pin**	**D pin**	**Units**
ESCON 50/5	3	0	2
BTS7960	2	4	2
TMC2208	0	7	2
AS5600	0	3	2
MPU-6050	0	2	2
NRF24L01	0	7	1
TOTAL	10	39	

What is shown in the Table 4.8 is an initial estimate of the required connections. The number may increase if decided to make further connections with pins that were not considered. In order to guarantee a sufficient number of pins in the microcontroller, a 40% increase to the calculated numbers was imposed. The number of pins required increases to 14 analog and 55 digital pins, some of which are capable of generating PWM signals and supporting I^2C communication.

As a result of the above considerations, the **Arduino Mega 2560 Rev3** [46] was chosen as the microcontroller. It has 56 digital pins, 15 of which are also PWM, and 16 analogue pins. If additional PWM pins are needed, it is possible to use simple digital pins and impose a PWM trend via code. It supports UART, SPI and I^2C

communication. The clock speed is $16MHz$. It has a 10-bit analogue-to-digital converter, i.e. an analogue signal can be converted to a digital value between 0 and 1023.

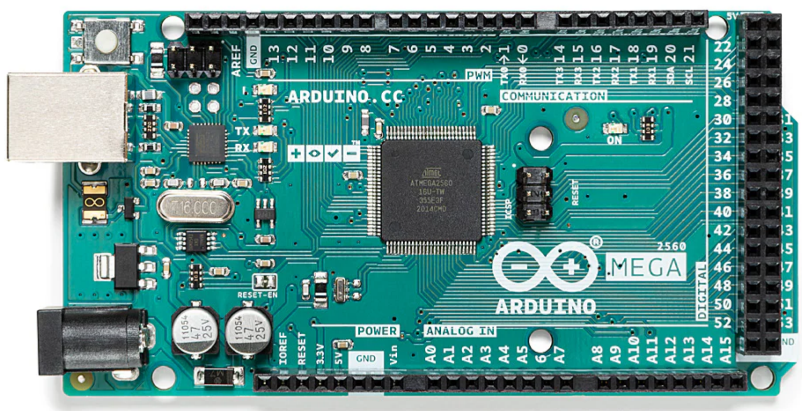

Figure 4.18: Arduino Mega 2560 Rev3.

Since no real-time image processing or forecasting is included in the control strategy, the Arduino's computing power was deemed sufficient. Viable alternatives for higher power computation can be found in Raspberry Pi and STM32 boards.

4.2.14 Positioning of the electronics

A key point in the development of the design was the placement of the electronics inside the rover. The structure has a internal complex shape and does not allow intuitive positioning of the electronics. An intrinsic problem in the design is that there are empty spaces that cannot be occupied. An example of this is the space inside the pendulum, which must be left free for the positioning of the CMGs to perform the gyroscopic manoeuvre. Finally, the aim must be to maintain as symmetrical a design as possible and with as low a centre of gravity as possible. After a series of attempts, it was decided to fit a box that could contain most of the electronic components mentioned so far. The electronics box is positioned above the differential box, i.e. in the centre of the rover.

Inside the electronic box the following components are placed: Arduino Mega Rev3, ESCON 50/5 drivers, TMC2208 drivers, BTS7960 drivers, NRF24L01.

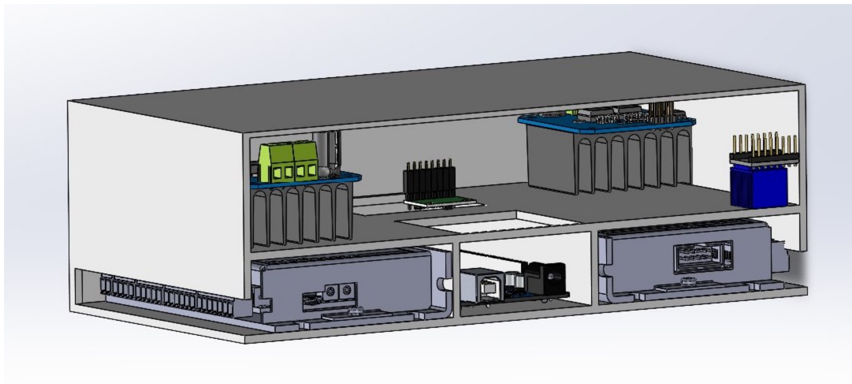

Figure 4.19: Section of the electronic case.

Bore slip rings have been placed on the main shaft of the rover. Their position is symmetrys respect to the differential box.
As said in Section 4.2.9, the first IMU sensor is placed under the differential box case, while the second one is placed in the internal part of the pendulum
Encoders HEDL and AS5600 are placed at the rear of the respective motors.

A further element of fundamental importance are the batteries that power the system. Their choice is addressed in Chapter 5, as they require a detailed evaluation that takes into account the system's various operating points. The batteries shown in this section are to be considered as the final choice.
Batteries constitute an important part of the system's weight. Placing them close to the electronics box would lead to an increase in the system's centre of mass, hence a reduction in performance. The final choice was to place them horizontally at the bottom of the pendulum side plates, as shown in Figure 4.20.

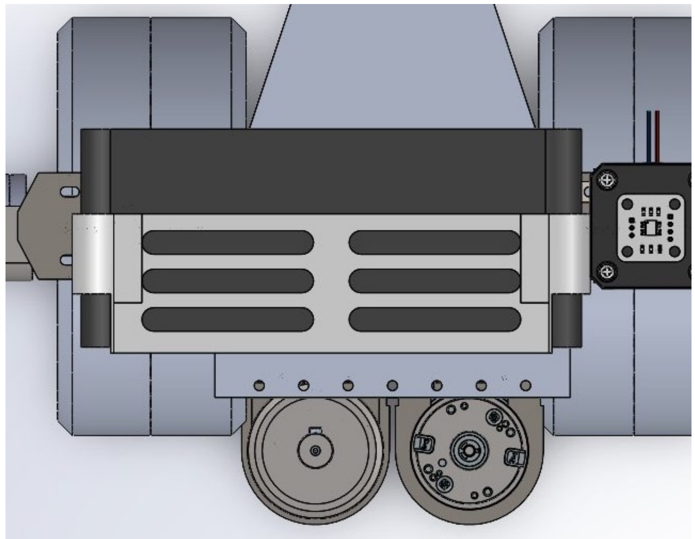

Figure 4.20: Battery position.

4.2.15 Electronic schematic

The schematic of the connections between the microcontroller, batteries and the other electronic components is shown below.
The connections between the components and the power source are regulated by auxiliary components (switches, capacitors, resistors, etc.) to limit and stabilise the input energy. The auxiliary components have not been modelled and need to be the subject of future advances.
The components using I^2C communication are connected to the SDA and SCL pins of the Arduino. The connection between the various sensors and the microcontroller is operated in parallel. When exchanging signals, the distinction between one component and another is made by means of an identification number.
Connections with analogue signals and connections with digital signals are highlighted.

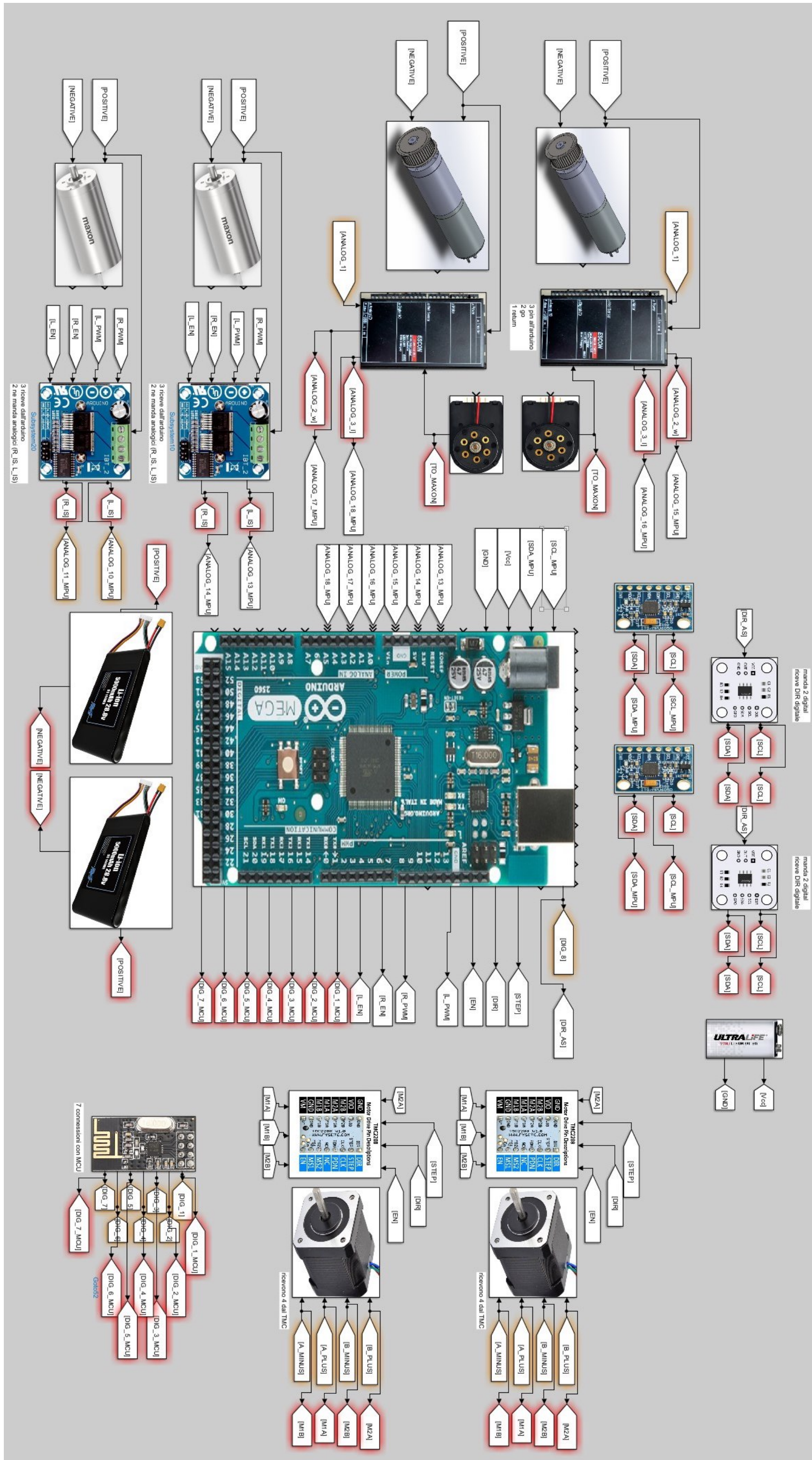

Figure 4.21: Scheme of the electronic network.

4.2.16 Considerations on vision sensors

A limitation due to the design is the implementation of sensors for image acquisition. Since the shell is continuously rotating, it is not possible to attach cameras externally without them ever coming into contact with the ground. Furthermore, it would not be useful to place cameras on the pendulum as image acquisition would become ineffective if an opaque shell was implemented. An evaluated solution is to insert cameras in the internal part of the shell. Vision can be performed through apposite holes placed on the shell, hole size depend on the camera lens diameter.

A first critical issue with this model is the impossibility of connecting devices to the microcontroller: the shell is constantly in relative rotation with respect to the electronics box. Another problem with this setup is that it is necessary to implement more than one camera to capture images of the trajectory. In fact, the continuous rotation of the shell results in a constant changing frame for each camera. Since the objective is to capture the image of the path in front of the robot, at least four cameras are required.

The implementation of vision sensors would require more powerful microcontroller for image processing.

4.3 Mechanics

After having carefully refined the electronic part, the mechanical part was developed. The choices seen in the previous part are still important in this section. In fact, knowledge of the electronics made it possible to estimate the additional weight and thus better size the structural components. In addition, changes have been made to include the batteries in the side plates of the pendulum.
The purpose of this part is to deal with the adjustments made to the previously modelled components to withstand the loads and the choice of materials. The arrangement and assembly functionality of the sub-assemblies are also analysed. Finally, a summary of the parts to be constructed and the final position of the centre of mass is presented.

4.3.1 Main shaft of the rover

This is the shaft that connects the pendulum to the spherical shell. Its task is to withstand the loads generated by the actuation of the motors in order to transmit the desired motion and torque to the spherical shell.
The two situations that must be considered when sizing the shaft are static load stress and fatigue bending moment stress. Situations in which shaft is damaged by torsional moment never arise because the shaft does not have fixed interlocks. Torques are always transmitted to the ball and never come to affect the shaft.

The first configuration is the static load configuration, i.e. when the rover is stationary and the shaft has to withstand the bending due to its weight and the weight of the pendulum. It can be formalised with a beam with two bearings at both ends and a load normal to the axis acting at the centre of the beam.
From [2], it is assumed the mass of the pendulum to be $m_p = 16kg$. The diameter of the previous modelled shaft is $d_{sh} = 15mm$. Assuming a shaft mass of $m_{sh} = 1kg$ and approximating shaft length to $l_{sh} = 0.5m$, the tension due to bending can be computed.

$$\begin{cases} M_b = \frac{m_p + m_{sh}}{2} \, \frac{l_{sh}}{2} \, g \\ W_b = \frac{\pi \, d_{sh}^3}{32} \\ \sigma_b = \frac{M_b}{W_b} \end{cases} \tag{4.5}$$

Where M_b is the bending torque, W_b is the flexural strength modulus and σ_b is the bending stress. The final tension is computed as $\sigma_b = 62.9MPa$. The action of the gyroscopic maneuver can be accounted as an additional bending moment acting on the shaft. In [2] the maximum CMG computed torque is $\tau_{G_{MAX}} = 25.82Nm$. Including $\tau_{G_{MAX}}$ in M_b computation, the maximum tension is computed as $\sigma_b = 140.8MPa$. By selecting a safety coefficient of 1.5, the minimum yied strenght to select is $\sigma_{yield} = 211.3MPa$.

A fatigue situation arises when the shaft is subjected to cyclic loads over time. Since the shaft and pendulum are constantly in relative rotation, the weight of the shaft can be described as a beam subject to alternating load. In particular, it can be calculated that medium tensions are $\sigma_m = 0$ and alternate tensions are $\sigma_a = \sigma_b$.
Following the Wholer Curve, no fatigue failure is expected for alternating stresses below the fatigue limit stress. Assuming $\sigma_{limit} = 0.5 \, \sigma_{UTS}$, fatigue failure is not expected for materials with $\sigma_{UTS} > 2 \cdot 62.9MPa$.
From these analysis, a steel can easily satisfy the computed requirements.

After testing the strength of the shaft, modifications were made to the shell mounting system. In the previous design, it was planned that the interlocking would take place by screwing in two cross joints.
Since the shaft and the shell are constantly subjected to rotation, the thread could become loose. A more reliable method of assembling the structure was developed. Shaft was reduced to a final length of $l_{sh} = 472mm$ and two holes near the shaft ends were added. Main shaft and cross joints are fixed by two fixing screw.

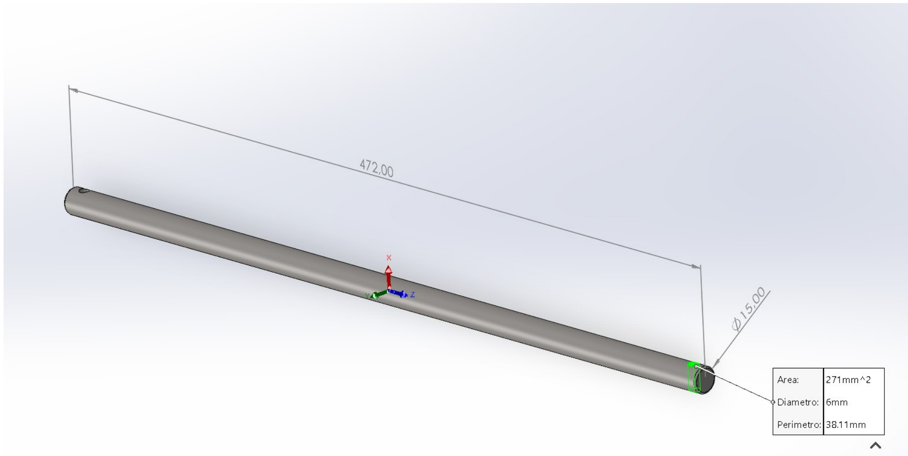

Figure 4.22: Main shaft final dimensions.

4.3.2 Cross joints

As mentioned in the previous paragraph, the cross joints were also modified to increase the reliability of the connection to the main shaft. A further objective of the revision was to simplify the assembly of the cross joint and the pendulum system to the spherical shell.
In the new version of the cross joint, the connection to the spherical shell is performed by means of fewer screws and only requires drilling into the shell at the screw entry points. In addition, the presence of a slot to accommodate the main shaft allows the following steps to be followed when assembling the rover:

- Firstly, the cross joint must be attached to the lower half of the spherical shell
- The main shaft and pendulum assembly can then be placed in the appropriate slots
- After securing the shaft by means of screws, the rover can be closed by fixing the upper part of the shell to the remaining holes in the cross joint

The hole in the centre of these components is used to allow the cables from the bore slip rings to pass through.

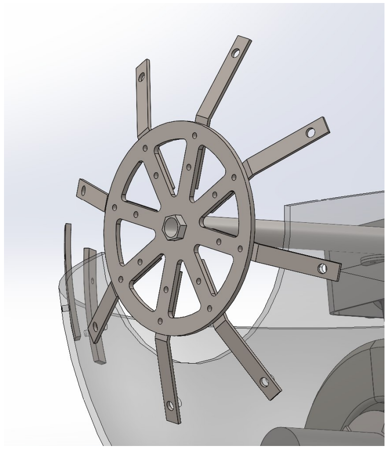

Figure 4.23: Initial cross joint.

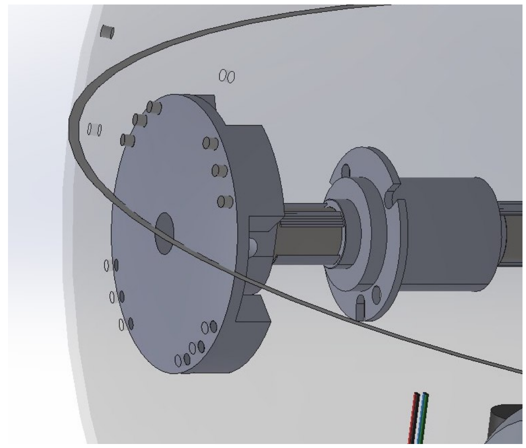

Figure 4.24: Final cross joint.

Hole sizing was addressed for the fixing screw junction.
Defining the material resistance, the geometry of the components and a safety factor it is possible to compute the minimum screw diameter using Formulas 4.6 and 4.7 derived from textbooks. Maximum load condition was considered for the sizing. P_{eq} is the equivalent weight force when τ_G is acting. σ_{amm} and τ_{amm} are stress values that define the diameter minimum size d_{min}.

$$\begin{cases} P_{eq} = (m_p + m_{sh})\, g + \frac{4\,\tau_G}{l_{sh}} \\ \sigma_{amm} = \frac{\sigma_{yield}}{CS} \\ \tau_{amm} = \frac{\sigma_{amm}}{2} \\ d_{min} \geq 0.92\sqrt{\frac{P_{eq}}{\tau_{amm}}} \end{cases} \tag{4.6}$$

imposing a screw diameter d, the following relations must be satisfied:

$$\begin{cases} \tau = 0.85\,\frac{P_{eq}}{d^2} \\ \sigma = 1.273\left(\frac{4}{3}s_f + d_{sh}\right)\frac{P_{eq}}{d^2} \\ \tau < \tau_{amm} \\ \sigma < \sigma_{amm} \end{cases} \tag{4.7}$$

Initial data and final values are reported in Table 4.9.

Table 4.9: Data and results of screw sizing.

DATA		
m_p	$16kg$	Pendulum estimated mass
m_{sh}	$1kg$	Shaft estimated mass
τ_G	$25.82Nm$	Maximum gyroscopic torque
l_{sh}	$472mm$	Shaft defined length
d_{sh}	$15mm$	Shaft defined diameter
s_f	$7.5mm$	Cross joint section thickness
CS	2	Safety coefficient
σ_{yield}	$250MPa$	Estimated yield strength
RESULTS		
d_{min}	$2.28mm$	Minimum screw diameter
d	$6mm$	Defined screw diameter

4.3.3 CMG group

A critical issue encountered in this assembly was the connection to the flywheel. In fact, it was initially assumed that connection between flywheel and CMG shaft was made via a feather key. The flywheel was finely dimensioned and its construction requires a high precision to meet inertial requirements. Creating an asymmetry to insert a keyway would be counter-productive as it would change the inertia parameters desired during modelling. It was therefore preferred to remove the recess for the key and change the tolerance between the two contact surfaces to achieve a junction through interference. Since the CMGs must rotate at constant speeds, the torsional forces acting between the two parts can never be high enough to induce noticeable relative motions.

A further issue was the expected assemblage with the CMG assembly. The dimensions that characterised the previous shaft design allowed for an efficient transfer of motion to the flywheel, minimising centripetal effects due to possible construction misalignments. However, the previously identified length did not allow assemblage with the motor. For this reason, it was necessary to increase the length of the shaft. With this new configuration, it was not possible to develop an assembly that provided all the fixing

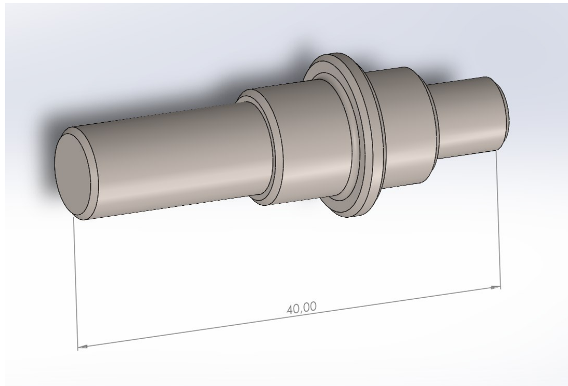

Figure 4.25: Final CMG shaft design.

connections between the motor and the CMG assembly permitted by the holes on the DCX 35 L.

A housing for the spinning motor was developed for the new situation. In this way, most of the connections to the motor are utilised and the connection to the CMG unit is ensured. In addition, the presence of a section that matches the motor shape prevents any eccentricity and vibration effects.
Finally, the case for attenuating viscous effects in the flywheel dynamics was also modified. Initially, four plastic components were planned that could be joined by means of dedicated C-shaped plates.

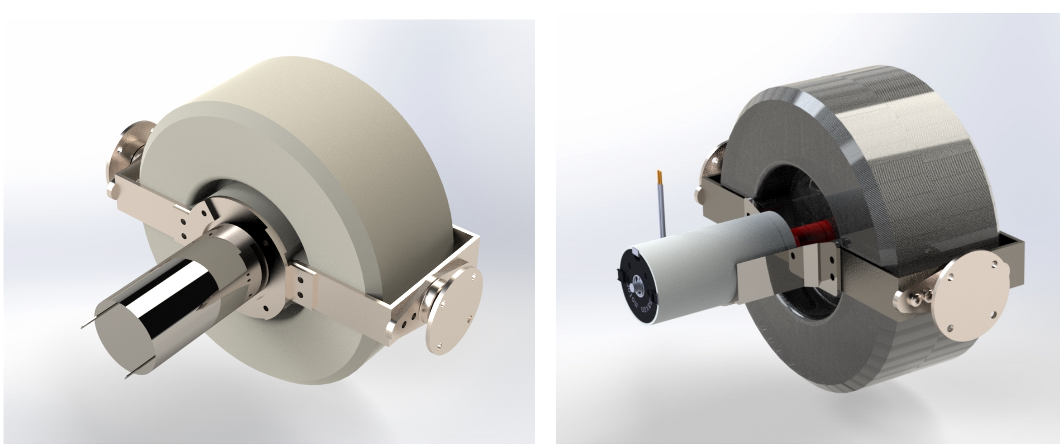

Initial CMG design. Final CMG design.

Figure 4.26: CMG comparison.

Since their function involves interference connection with the bearings (”SKF61800” and ”SKF61701”) to provide rotation of the flywheel, plastic is not suitable for this role. A compromise between cost, weight and mechanical properties suitable for this purpose led to the selection of an aluminium alloy as material. In addition, it was decided to make the case consisting of only two units, to make assembly easier.
The CAD of the new parts compared with the previous versions and the new CMG unit are presented in 4.26.

4.3.4 Connection plates between CMG and pendulum structure

Two types of plates are required for the connection between the main structure and the CMG assembly. The **First Connection Plate**, are used to integrate the stepper motors to the CMG assembly. The **Second Connection Plate** include the entire gyro assembly to the pendulum.

First Connection Plates have been modified to remove the rear support of the CMG assembly. Constantly powering the stepper motor allows the desired angle of inclination to be maintained. Continuously feeding the angle via the motor reduces the oscillations that could affect the CMG assemblies along the tilting axis. It is therefore possible to remove the rear supports that represented a mechanical limiter for the tilting angle of the CMGs. Holes have been added to improve the connection with the Second Connection Plates. To facilitate assembly, the First Connection Plates have been divided into four separate pieces in contrast to the initial two pieces.

The Second Connection Plates have the task of securing the previously treated plates to the pendulum. As the modifications to the CMG assemblies have led to an increase in weight due to the metal materials used, it was decided to increase the stability of the seal by thickening the plates and increasing the joint points. This makes the structure more stable and prevents the formation of oscillations that would be transmitted from the CMG assembly to the main plates of the pendulum. The additional costs resulting from these modifications were estimated to be negligible.

The changes are presented in Figures 4.27 and 4.28 with comparisons to the previous asset. Finally, 4.29 shows the FEM for the maximum load condition. A detailed analysis about the maximum load is presented in Section 4.3.5.

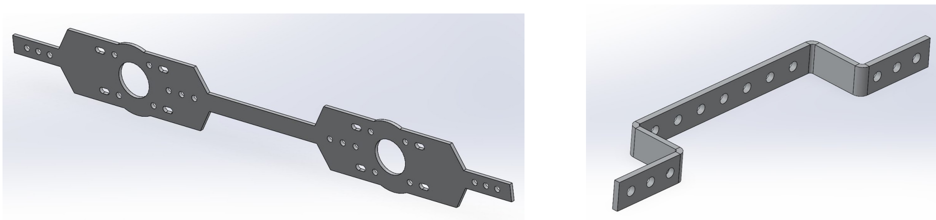

(a) (b)

Figure 4.27: Initial First (a) and Second (b) Connection Plates.

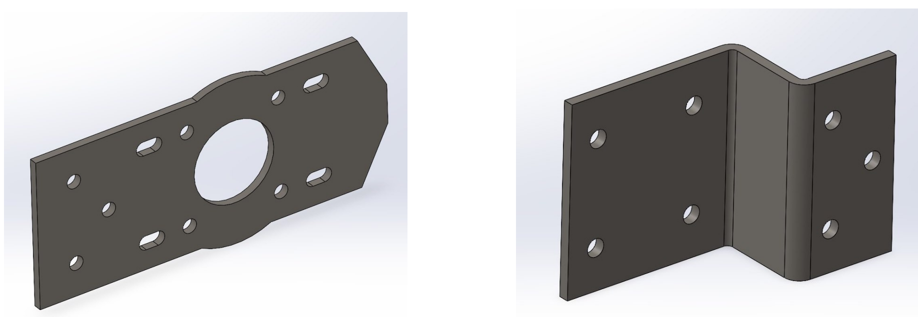

(a) (b)

Figure 4.28: Final First (a) and Second (b) Connection Plates.

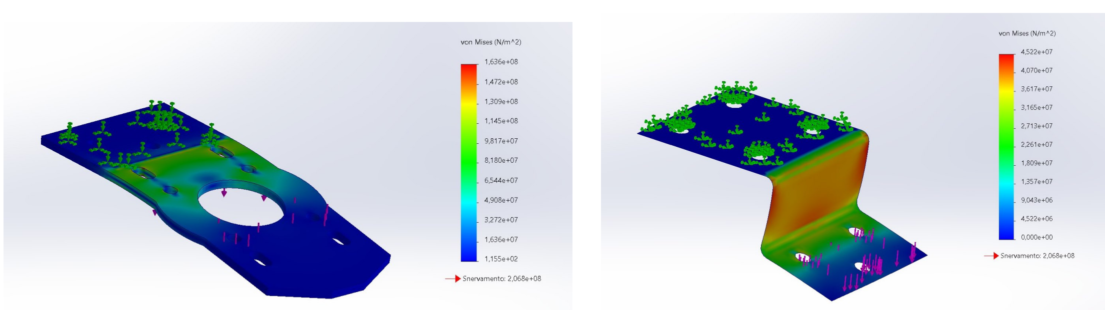

(a) (b)

Figure 4.29: Final First (a) and Second (b) Connection Plates FEM.

4.3.5 Pendulum main plates

These are the main components of the pendulum structure. Their function is to support the main motors and gyro units. Their connection with the differential box is performed through bearings, in order to guarantee the lateral inclination.
They must be sized to support the weight of the pendulum in different configurations. Furthermore, they must be able to withstand the additional load provided by the implementation of the gyroscopic torque.

The starting point is the previously modelled plate and appears as a light triangular structure:

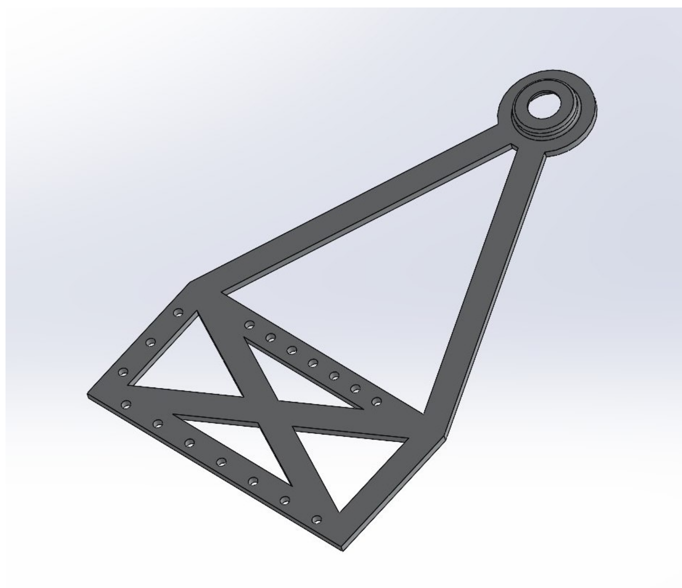

Figure 4.30: Previous design of main plates of the pendulum.

The shape was developed to be a compromise between the connections that must be made, the practicality of the connection to the differential box and the minimum amount of material required to fulfil its intended function.

The maximum load situations that the plates must withstand need to be defined. There are two main load situations.
The first is the static load, where the pendulum is in the standstill position.
The second one when implementing the gyroscopic manoeuvre. This configuration

involves the pendulum inclined at 90° with respect to the normal to the ground, and the boost due to the gyroscopic torque is added to the total load to be withstood.

The first situation can be easily assessed by computing the normal stress caused by the weight of the pendulum. The weight of the pendulum must consider the additional weight coming from the design changing. Since the structure is symmetrical, the distribution of forces is homogeneous.

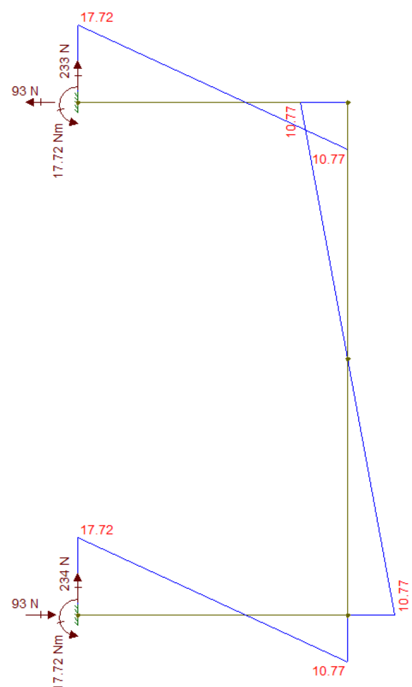

Figure 4.31: Ftool derived behaviour of the torque acting on the pendulum structure.

The normal stress suffered by a single plate is:

$$N = \frac{m_P\, g}{2} \tag{4.8}$$

In the second situation, the stress derives from the bending moment. The moment required to hold the pendulum in position can be calculated knowing mass and position of the COM of the pendulum. L_P is the distance between the junction with the differential box and the barycenter of the pendulum. The action of τ_G is to increase the torque acting on the shell to overcome the step.

The final formula is:

$$\tau_P = L_P\, m_P\, g + \tau_G \tag{4.9}$$

In this configuration, the pendulum can be interpreted as an hyperstatic structure. Using the software Ftool, it was possible to compute the constraining reactions of the structure shown in Figure 4.31.
Since bending torque generates worst stress conditions, the following analysis were conducted hypnotising pure bending torque acting on each plate. The torque considered on a single plate was half of the maximum value obtained from Equation 4.9 since the structure is symmetrical.
This is a conservative approach and it was adopted since structure sizing was not ended yet. Structure sizing affects the final required τ_G for the step climbing, thus it is important to size the structure in case higher torques are applied.

The analysis was carried out by focusing on the most important stress case, i.e. the bending moment stress. It was possible to perform a FEM analysis on the CAD component using the appropriate SolidWorks tool.
During bending moment application, the plate that bears the largest stress is be the one positioned on the top. This is because the stretched fibres are characterized by abrupt geometry variation. The vertical force is distributed equally between the bearings even in the 90º pendulum situation.

By setting an aluminium alloy with $\sigma_{yield} = 290MPa$ as material, the critical stress is reached and exceeded at several points on the plate. It can be observed that a stress concentration occurs at the shoulder points designed for bearing insertion.

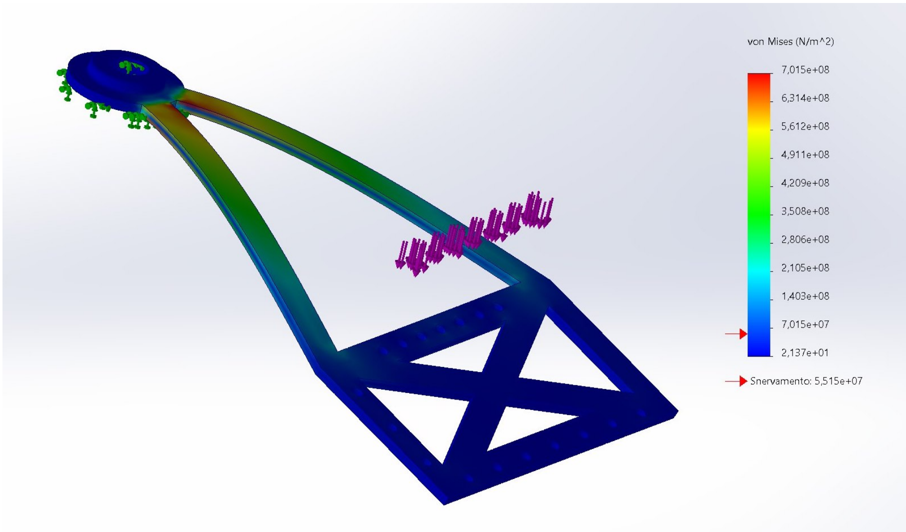

Figure 4.32: FEM analysis on the initial plate under maximum load conditions.

Several observations can be drawn from the FEM analysis.
The plate exhibits sudden changes in geometry, which results in a significant increase in tension at the corresponding points. One solution is to make the plate geometry more compact and linear.
The plate has several areas with no material. The presence of holes generally corresponds to a weakening of a structure, so it is necessary to minimise their presence in order to maintain high load-bearing performance. The holes required to connect with the plates discussed in the previous section are necessary and therefore cannot be removed. The triangular-shaped areas can be removed as they are designed with the aim of lightening the structure.
Finally, it is necessary to find a minimum thickness to keep the profile of the plate as regular as possible. This necessity is imposed because having a variable plate thickness would require more mechanical processing and thus a higher final cost for its production. In addition, it was planned to position the batteries on to the plates. A variable section would make their positioning unnecessarily difficult.

The removal of gaps and sudden changes in geometry resulted in the plate profile of Figure 4.33.

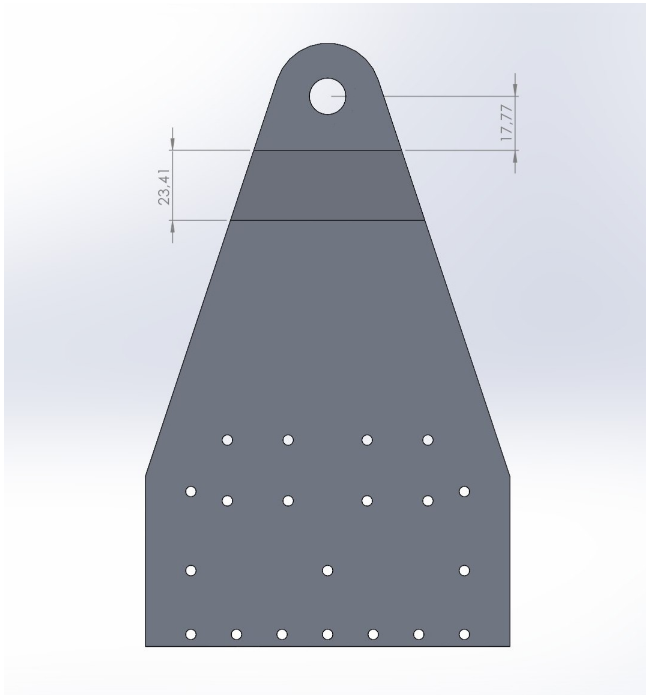

Figure 4.33: Frontal view of the pendulum plate. Holes were removed and a more compact geometry was provided in correspondence of the differential box junction.

To define the appropriate thickness, more in-depth computations were carried out.
Bending moment profile is linear and starts from the connection areas with the CMG groups and ends when it reaches its maximum value at the joint connection. The most stressed section by bending moment is the one at the bearing connection. Since maximum torque value is known, the flexural strength modulus was constructed as function of the thickness of the section s.
Imposing a safety coefficient $CS = 1.8$, $s = 7mm$ results as the final thickness value.
This thickness was imposed constant for all the sections near the junction, in order to avoid abrupt geometry variations.

To identify the best thickness to be used for the remaining sections, a model describing the variation of the width of the sections along the axis of symmetry of the plate was developed using Excel.
Section variation was accounted to compute the corresponding flexural strength modulus. As before, thickness was accounted as a variable to tune in order to

decrease the stress acting on each section. Through a trial-and-error approach, $s = 3mm$ was selected as the thickness.

The thickness of $3mm$ is suitable for most of the stressed sections. The admissible stress $\sigma_{amm} = 161MPa$ condition imposed by the selected CS is respected by the majority of the plate sections. The sections that exceed the admissible strength in Figure 4.34 are the same represented in the $23.41mm$ section in Figure 4.33. In this section, a linear transition is from $s = 3mm$ to $s = 7mm$ is operated. The stress profile is now correctly sized on each section of the plate. Final stress behaviour is represented in Figure 4.34.

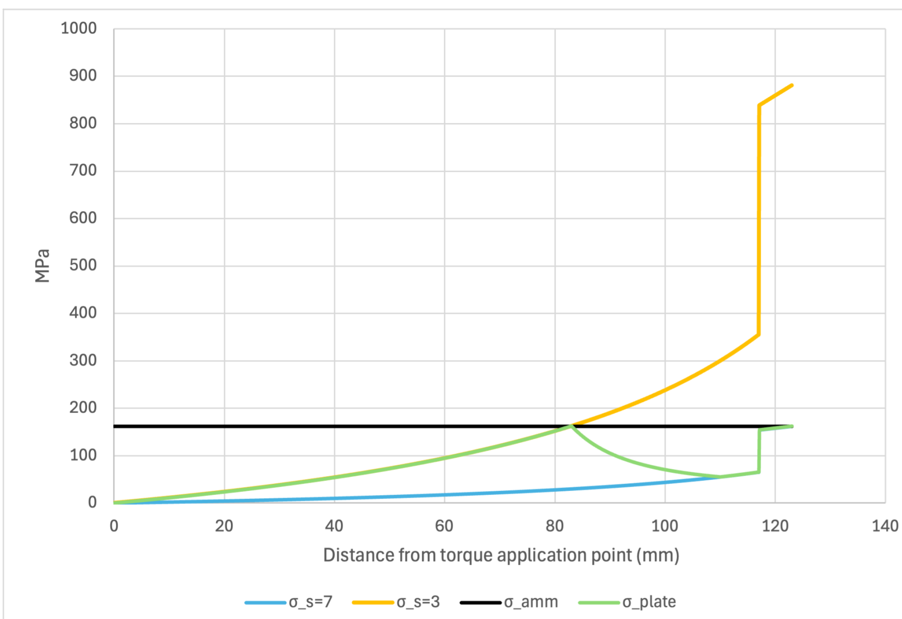

Figure 4.34: Stress behaviour for different thicknesses of the plate. It can be seen how the σ computed using thickness $s = 3mm$ exceeds the admissible stress.

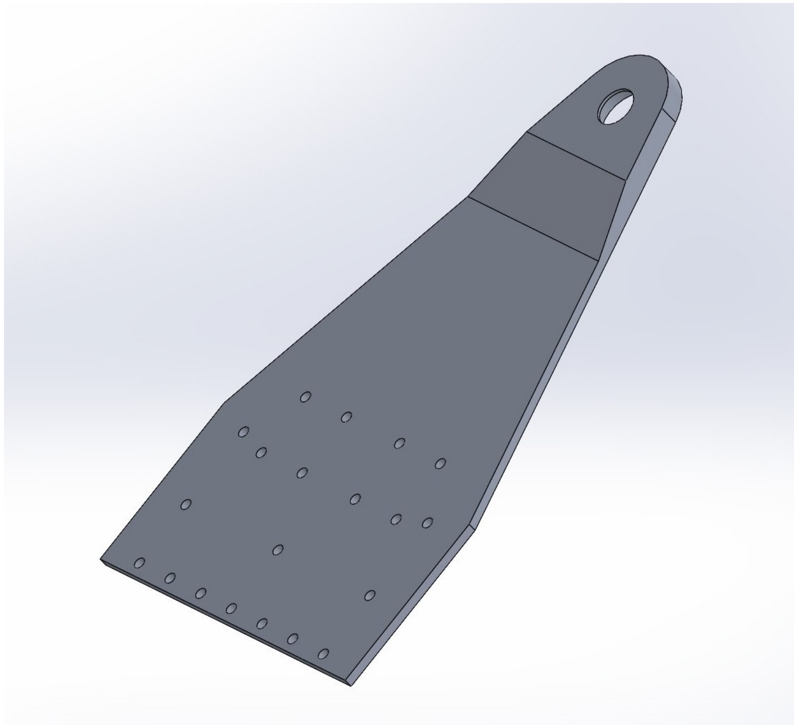

Figure 4.35: Isometric view of the final designed plate. It is possible to notice the thickness variation.

Final design of the plate is shown in Figure 4.35. FEM analysis in SolidWorks shows that the stress values never exceed the admissible strength.
The final result of the modelling is a plate capable of withstanding all load situations of the rover. In addition, the considerations were also developed by considering construction costs.
Subsequently, additional holes were provided for the positioning of the batteries by means of dedicated housings. As confirmed by further FEM analysis, holes of this type do not significantly affect the strength of the plate.

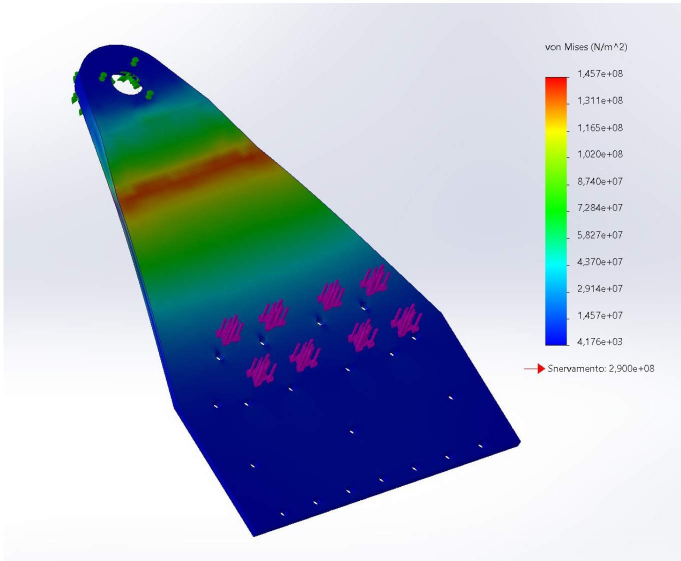

Figure 4.36: FEM analysis of the final plate in maximum load conditions

Table 4.10 resumes the used values and results for the sizing of the plates.

Table 4.10: Data and results of main pendulum plate sizing.

DATA		
m_P	$16kg$	Pendulum estimated mass
L_P	$0.12m$	Pendulum estimated barycenter distance
τ_G	$25.82Nm$	Maximum gyroscopic torque
CS	1.8	Safety coefficient
σ_{yield}	$290MPa$	Strength of the selected material
RESULTS		
τ_P	$44.65Nm$	Maximum torque acting on the pendulum
τ_{Plate}	$22.33Nm$	Maximum torque acting on a single plate, half of τ_P
σ_{amm}	$161MPa$	Ratio between σ_{yield} and CS

4.3.6 Planned parts for 3D printing

The components planned for 3D printing are discussed below. These are not involved for structural implementation and motion transmission, therefore do not require high resistance. Since they are constantly in contact with electronic components, the material used must be able to withstand the temperatures without deformation or damage. For the selected electronics, temperatures above 80ºC are not expected; materials such as ABS can withstand these conditions.

Battery case. The chosen batteries are a pair of **MaxAmps Li-Ion 5000 8S1P 28.8V**. The dimensions, which can be found in the datasheet [47], are 169x22x74mm. Enclosures have been developed to hold them to the pendulum plates via bolted connections. The enclosures have slots to facilitate temperature dissipation. The choice of the power supply is addressed in Chapter 5.

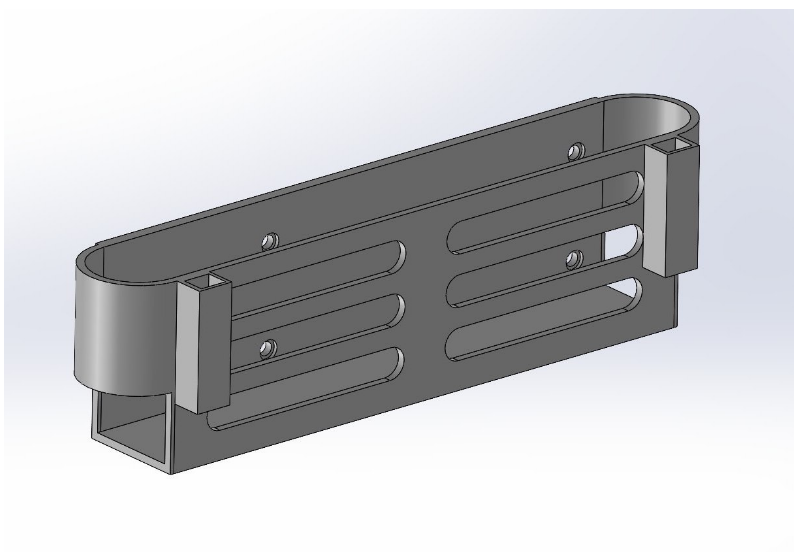

Figure 4.37: Battery case.

Differential box case. A top and bottom closure is designed to protect the differential housing gears.

Electronics case. Section 4.2.14 named the electronic components that are placed above the differential case. The function of this box is to collect and hold the planned electronics. The box is developed in two planes: the first contains the microcontroller

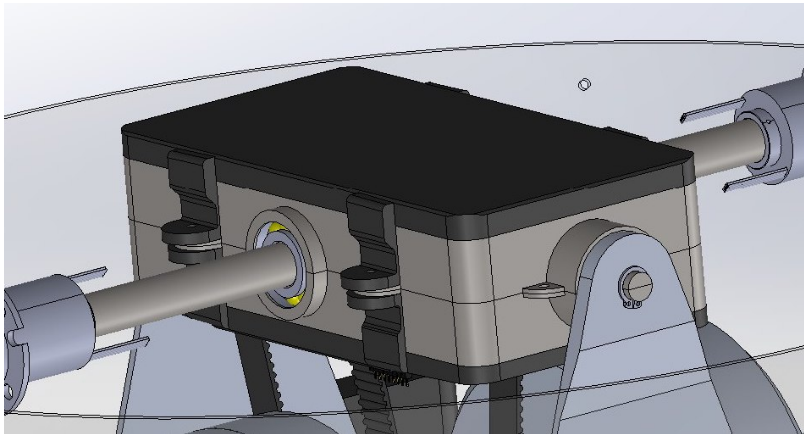

Figure 4.38: Differential box case.

and Maxon drivers, the second the remaining components. Holes have been provided for the passage of wires. The case was already shown in Figure 4.19.

4.3.7 List of components to be produced

Below are the parts to be produced with number of units, weight, and their selected materials

Table 4.11: List of components to produce

Components	**Units**	**Weight**	**Material**
Main shaft	1	$644g$	Structural steel
Cross joint	2	$120g$	Aluminium alloy
Differential box shell	2	$269.7g$	Structural steel
Lateral shaft	2	$126.3g$	Unalloyed steel
Counterweight	1	$111g$	Ferrous stainless steel
Pendulum main plate	2	$157.4g$	Aluminium alloy
First connection plate	4	$42.67g$	Forged stainless steel
Second connection plate	4	$39g$	Forged stainless steel
Stepper plate	2	$7.5g$	Ferrous stainless steel
Tilt bearing plate	2	$17.3g$	Ferrous stainless steel
Tilt flange	2	$41.8g$	Ferrous stainless steel
Tilt flange low	2	$18g$	Ferrous stainless steel
Tilt bearing plate low	2	$32.5g$	Ferrous stainless steel
Motor plate	1	$348.6g$	AISI304 steel
Motor fixing plate	2	$11.5g$	Forged stainless steel
Motor collar	2	$62.5g$	Forged stainless steel
Motor junction plate	2	$3.8g$	Forged stainless steel
CMG tilt plate	4	$52.7g$	Forged stainless steel
Spinning motor housing	2	$50.5g$	AISI1020 steel
CMG case first half	2	$334.3g$	Aluminium alloy
CMG case second half	2	$518.4g$	Aluminium alloy
CMG rear junction plate	2	$36.5g$	Ferrous stainless steel
CMG shaft	2	$19.02g$	Ferrous stainless steel
Flywheel	2	$3,459g$	Forged stainless steel

4.3.8 List of components to be purchased

The mechanical components that can be purchased are listed below. The list includes the selected components, the number of units required and a brief description of their implementation. The low costs and small footprint led to the selection of bearings by means of largely precautionary calculations.

Table 4.12: List of purchasable components

Components	Units	Description
61800-2RS-SKF bearings	4	Between main shaft and differential box and
W618-8-SKF bearings	2	Between carted and shaft CMG
61701-2RS bearings	4	Between CMG and pendulum structure
6202-2RS-SKF bearings	6	Between main shaft and differential and lateral shaft and differential
ALS-014-R joint	2	Used to connect spinning motor to CMG shaft
POGGI 3MGT3 belts	2	Used to transmit motion from lower puleys to upper pulleys
GPT44GT3150-A-N12 pulley	2	Welded to pendulum motor gearhead
GPT44GT3150-A-N15 pulley	2	Welded to lateral shaft of differential box
BSM2030 miter gear	3	Used for bevel connection in differential box
Acrylic cupola 500mm	2	External shell of the rover

4.4 Final design summary

This chapter covered the additions and changes that led to the final design.
Each component was reviewed so that the working conditions would not lead to damage or misalignment of the structure. The practicality for assembly was also checked to ensure that no misprints were present that would limit the feasibility of assembling the components. The components that have not been mentioned so far

have been checked and validated but did not require further modifications. It was therefore deemed unnecessary to include them in the presented work.
For each component to be produced, tables with the appropriate tolerances have been drawn up. The acrylic shell serves to show how the inner mechanism works. A rubber membrane or a shell of a different material and finish is required to have sufficient friction with the ground for advancement.

A key point in achieving the expected performance was the positioning of the system's centre of mass. For optimum operation, the COM of the pendulum and the system must be positioned along the axis of symmetry of the sphere perpendicular to the ground. A misprint still present required the stepper motors to be arranged on the same side. To redistribute the weight appropriately, it was sufficient to reverse the position of one of the two tilting motors. This modification leaves the gyro operation unchanged, the only difference from the previous configuration being in the direction of the spinning and tilting speeds.

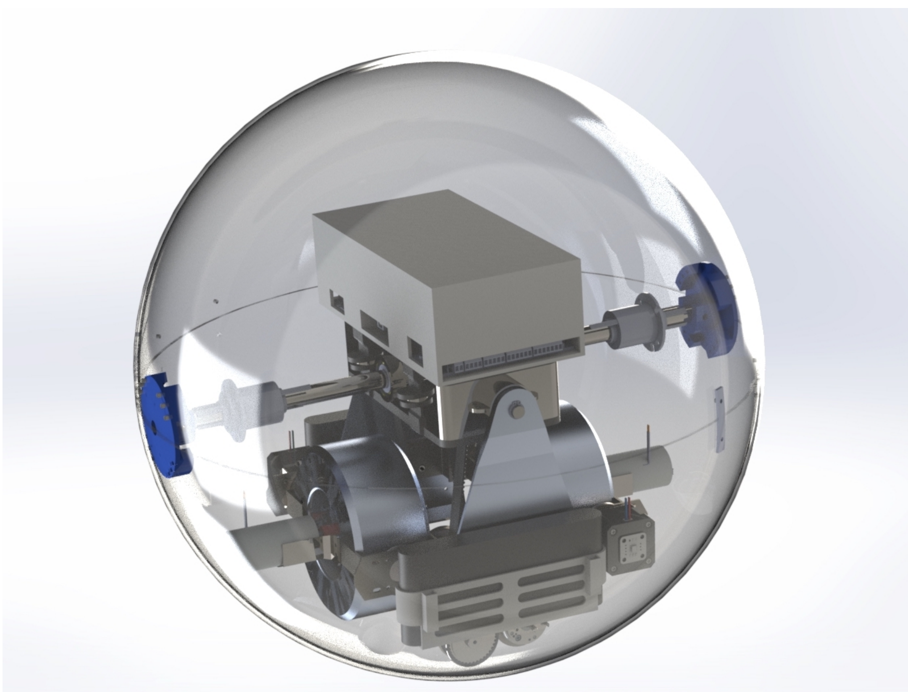

Figure 4.39: Final design of the spherical rover.

4.5 Costs table

Below are the costs of the components to be purchased and the units:

Table 4.13: List of all the components and final costs

Components	**Units**	**Cost**
Maxon RE 40 + Planetary Gearhead 42 C + HEDL 5540	2	€958.28
Maxon DCX 35 L	2	€349.25
Nema 17 ($40Ncm$)	2	€9.60
Bore slip ring H1532	2	€50.00
Arduino Mega Rev3	1	€42.00
Maxon ESCON 50/5	2	€283.99
BTS7960	2	€14.18
TMC2208	2	€5.56
MPU-6050	2	€5.99
AS5600	2	€15.99
NRF24L01	2	€6.00
ALS-014	2	€14.61
3MGT3	2	€11.23
GPT44GT3150-A-N12	2	€36.98
GPT44GT3150-A-N15	2	€36.98
BSM2030	3	€45.37
61800-2RS-SKF	4	€15.02
W618-8-SKF	2	€17.81
61701-2RS	4	€3.22
6202-2RS-SKF	6	€5.28
TOTAL		€4,067.71

Chapter 5

Results and discussions

As mentioned in Chapter 1, the study performed in the thesis was divided into two distinct parts. The final chapter of this thesis provides a summary of the topics covered in the next subdivision including the obtained results.
In Part 2, the main topic is about the modelling and the control strategies that were implemented after the final design was individuated. This part starts with considerations about power duration depending on the different main situation of the rover. Then, multibody and analytical modelling are presented in order to derive simulations of the plant. Finally, different control strategies are shown, depending on the desired objective and the approximations operated.

5.1 Performance analysis

After the choice of the electrical and mechanical components, the final values characterising the rover can be computed. In Table 5.1, information about coefficients and goals are reported too. From these information it is possible to study the rover main operations and relative power consumption.

Rover principal tasks are:

- Forward movement of $2.5m/s$ on a plane
- Forward movement of $2.5m/s$ on a $15°$ slope
- Step climbing through CMG maneuver actuation

Table 5.1: Data of the final design and goals of the project. Motor and gearhead values are taken from datasheet [33] [34].

ROVER DATA		
M_S	$6.74kg$	Shell + differential system + electronics mass
m_P	$15.65kg$	Pendulum mass
a	$9.14cm$	Barycenter position of the SR
L_P	$13.57Nm$	Barycenter position of the pendulum
COEFFICIENTS		
η_D	0.98	Differential box efficiency
η_B	0.95	Belt efficiency
η_G	0.72	Gearhead efficiency
η_M	0.91	Pendulum motor efficiency
PENDULUM MOTOR DATA		
k_T	$30.2\,{}^{mNm}/_{A}$	Torque constant
k_V	$317\,{}^{rpm}/_{V}$	Speed constant
R_a	0.299Ω	Terminal resistance
GOALS		
R_S	$25cm$	Radio of the sphere
h	$10cm$	Maximum height of the step
ω_S	$10rad/s$	Nominal angular speed
α	$15°$	Nominal angle of the slope
T	$1h$	Nominal operation time

From each of these situations it is possible to derive the torque acting on the pendulum. By considering all the efficiencies of the single elements of the transmission, a value of current can be deduced by implementing the motor constants. Knowing the required current it is possible to compute the power consumption.
For the CMG, the consumption is due to all the motors working at the same time to climb a step. Thus, it can be derived the consumption depending on the number of steps to climb.

The function to compute the required charge was constructed by imposing a trade-off of 75% between planar and slope situation. Also, the charge consumption considers the number of steps N to be climbed and the continuous consumption of the stepper

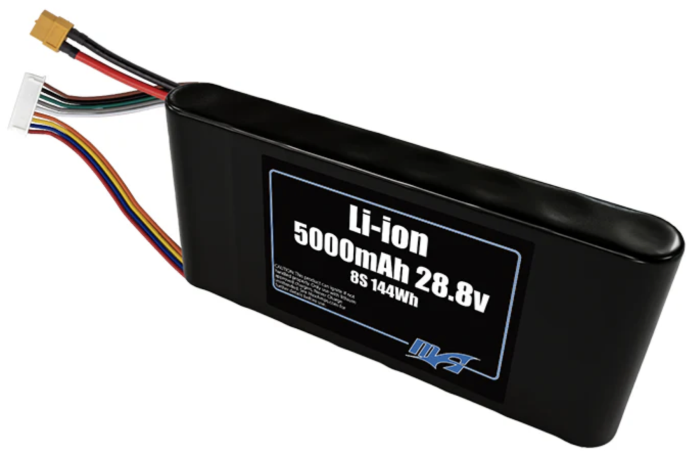

Figure 5.1: MaxAmps chosen battery.

motor.
The final formula is:

$$C = 2 \cdot (I_{plane} \cdot 0.75\,t + I_{slope} \cdot 0.25\,t + I_{stepper} \cdot t + I_{CMG} \cdot N) \tag{5.1}$$

By imposing the duration and number of steps it is possible to compute the required charge. For N=5 and t=1h, the final selected batteries were the **MaxAmps Li-ion 5000 8S1P 28.8v Battery Pack**. Voltage of the selected batteries is major than the maximum operating voltage required from the pendulum motor. The capacity of a single battery is 5Ah, an efficiency factor of 0.85 was included
For nominal conditions, the duration is about 48 minutes. The electronic is powered by a different battery, thus do not affect the formula of C.

5.2 Multibody plant definition

The study proceed generating the virtualization of the Rover in the Multibody form. Through the implementation of the software MATLAB, three different models of the plant were created in Simscape/Simulink environment. The three systems differ on the detail accuracy. The main one was generated as complete and high fidelity model, taking into account every designed component and relative motion among them. Second and third models were resulted after representing more pieces using the same File Solid. This approximation modifies part of the dynamics and the structure is described by fewer blocks. Changes were addressed with the objective to maintain the principal aspects of the simulation and to increase computational speed. In particoular, the third model was the result of extimely high approximation in order to obtain efficinet real time controlling using an external joypad.

After plant definition, open loop tests were performed in order to study different performance behavior of the three models. Different surfaces were generated to test the robot. The principal surfaces used are normal infinite plane, inclined plane and customized surface.
The imposition of a references signal was actuated through three different input. The step input was used to study the transient and stability performances of the rover by reaching different speed steps. The signal builder input block allowed to set a simple linear varying reference, to perform different speed profiles and curved trajectories. Lastly, a joypad controller was used as open-loop approach for live-control manipulation of the rover.

5.2.1 Dynamics equation

A considered approach was to derive a set of equation to describe the relation between pendulum angles and the dynamics of the rover. As seen in [2], starting from a dynamic description of the plant it is possible to simulate the behaviour of the system depending on external inputs.
The Euler-Lagrange equation have been derived to obtain the direct dynamics of the rover when applying input torques along the main pendulum angles. The system

accounts for the following variables:

$$\boldsymbol{q} = \begin{bmatrix} x & y & \theta_z & \theta_y & \theta_x & \alpha & \beta \end{bmatrix}^T$$

where $(x,\, y)$ are the position variables of the rover COM on a plane, $(\theta_z,\, \theta_y,\, \theta_x)$ are the roll-pitch-yaw angles of the sphere, and $(\alpha,\, \beta)$ are the pendulum angles. The system was described by four main boies that are shell, differential box, electronic case and pendulum. The values of masses and inertia were derived from the SW CAD files.
By computing and deriving the position vectors of the system bodiee, the Lagrangian equation $L = K - P$ can be obtained. A set differential equations can be derived by solving the lagrangian equation defined as:

$$\frac{d}{dt}\left(\frac{\partial L}{\partial \dot{q}_i}\right) - \frac{\partial L}{\partial q_i} = Q_i + \sum_j \lambda_j \frac{\partial \phi_j}{\partial q_i} \tag{5.2}$$

Non-holonomic constraints were included as imposition on the sphere movement. This is represented by the presence of the Lagrangian multipliers λ_j. By means of matrix calculations and substitutions, the final equations could be derived ignoring the unknown values of λ_j.
The final result is reported in matrix form:

$$\bar{\boldsymbol{M}}_1 \ddot{\boldsymbol{q}}_2 + \bar{\boldsymbol{M}}_2 \dot{\boldsymbol{q}}_2 + \bar{\boldsymbol{V}} = \bar{\boldsymbol{I}} \boldsymbol{u} \tag{5.3}$$

where

$$\boldsymbol{q_2} = \begin{bmatrix} \theta_y & \theta_x & \alpha & \beta \end{bmatrix}^T$$

$\bar{\boldsymbol{M}}_1$ and $\bar{\boldsymbol{M}}_2$ are the coefficient matrices of $\ddot{\boldsymbol{q}}_2$ and $\dot{\boldsymbol{q}}_2$ vectors, $\boldsymbol{u}$ is the input vector of torques applied on pendulum.

5.3 Controller design

Finally, a study related to the design of the controller was performed. The objective is to perform reference tracking of user-set values.
The control strategy starts from the elaborated forward movement controller developed in [2]. The values required from the controller have been tuned in order to be adapted to the current plant.
A controller to implement the lateral rotation of the rover was developed. The controller allows to set the desired angle of the pendulum respect to the normal direction of the main shaft by computing the required motor speeds. The controller was developed to reduce the oscillation in the tilting direction on sphere's shell caused by the movement of the pendulum. The maximum tilt angle depends on design limitation deriving from the contact between pendulum and main shaft, as shown in Figure 5.2:

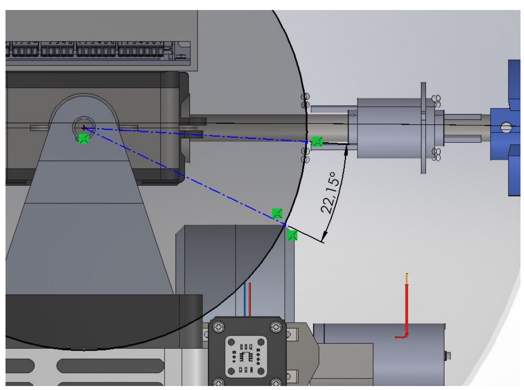

Figure 5.2: Maximum lateral angle.

A planar controller was defined by combining the two controllers. The resulting controller (Figure 5.3) is able to follow both the inputted linear velocity and angular references with zero steady state error. The structure is based on the kinematic equations that describe the motion relation between spherical shell, pendulum and motors at the differential box seen in 3.1.
Although the path of the rover is subject to the settling velocity of the input values, the trajectories are characterised by a smooth profile and positively respond to sudden input variations. Starting from the maximum inclination of the pendulum, it was derived the minimum curvature radii to be equal to $0.618m$.

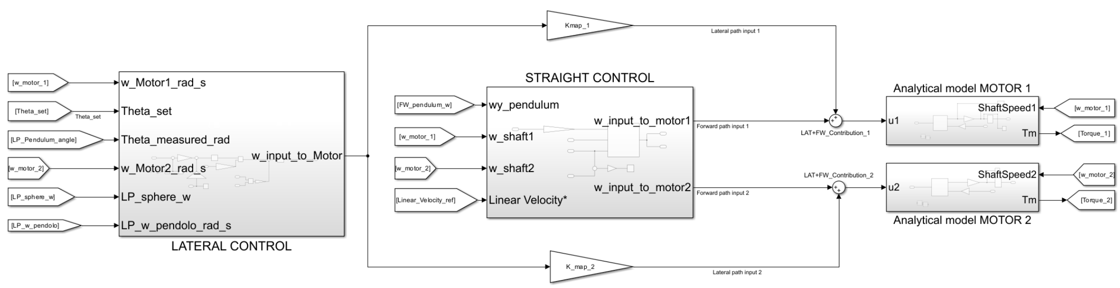

Figure 5.3: Scheme of the controller.

In table 5.2 the results of the performances are listed. It is important to remember that the final controller actuates a sphere that is subject to non-holonomic constraints. This implies that steering and forward velocity affect each other and the respective transients result higher respect to the independent applications.

Table 5.2: Results from the virtual model of the spherical Rover

Control typology	**Rise time**(s)	**2% settling time**(s)	**Overshoot**$(\%)$
Linear trajectory	5.09	9	3.25
Lateral angle	2.3	8	17.45

Tests on different path profiles were performed to test the responsiveness of the rover. In Figure 5.4 an example of circular trajectory is shown. After the settling of the inputted values, the rover presented a high adherence to the predicted trajectory.

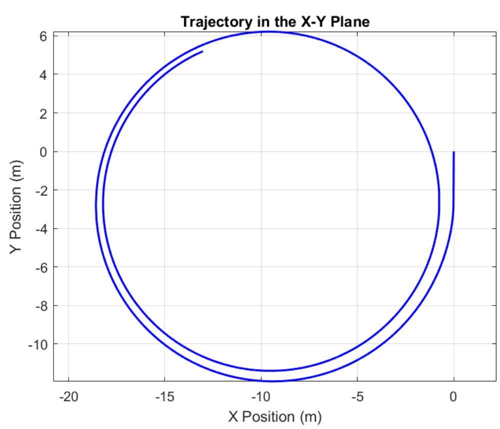

Figure 5.4: Circular trajectory in a planar control application.

Chapter 6

Future works

In this final chapter, possible future extensions and improvements to the presented work are discussed. The main future developments include the construction of the prototype of the rover, upload and correct the developed code on the microcontroller, implementation of vision sensors, laboratory tests and actuation using external joypad.

The costruction of the rover must pass through the selection of a company for the production of the specific components that have been modelled. It will be necessary to accurately define the dimensional and geometrical tolerances that can be performed during the production of high-precision components as the flywheels. It is expected that some components will slightly change depending on the production complexity and the material availability.
Material plays an important role for the production phase. Although resistance is an important factor that is affected by material, another important propriety that depends on it is the weight of each component. As elaborated in the dimension phase, weight of the system plays an important role. By varying the weight, the final COM changes. It would be possibile to correct the final barycenter position by strategically positioning specific weights.
A company will be commissioned for the assembly of the final rover. Several connections are realised through interference and require high reliability.
Finally, a different shell or a film must be applied to the rover. Acrylic has been chose to look through the shell and to analyse the behaviour of the sphere depending on the internal state of the pendulum. For a practical actuation, different materials

need to be considered in order to set appropriate friction values with the terrain.

After enhancing and stabilise the control strategy to be implemented, conversion from the Simulink/Simscape algorithm to an IDE code needs to be performed. Tool developed for this practical tusk have been created, however conversion always requires a human elaboration. Code must be accurately imported on the microcontroller in order to account the possible variations of the design after the construction part and structure misalignments.
Furthermore, filtering structures will be elaborated to correctly remove the effect of sensors noise acquisition and all the oscillations derived form the environment. Depending on the application, different apporaches of filtering can be implemented.

A system for external data acquisition will play an important role for the definition of the possible tasks that can be performed. Vision systems outputs are easy to interpretate for humans, however several factor limit this choice. The cameras shall be placed in the internal part of the shell, since the external surface is always rotating and periodically almost each point touches the ground. Cameras cannot be directly connected to the microcontroller since the relative motions would cause the twisting and breaking of the implemented wires. A wireless system implementing apposite microcontrollers such Arduino Nano combined with transmitters can be a possible solution.
The placement of cameras would require a glass or plastic protection. However, the presence of locally non-smooth small geometry and the continuous rotation may lead to a significant presence of dust and dulling of the initial transparency of the provided protection.
Furthermore, the continuous rotation of the shell implies that almost every point - except for the poles on the rotational axis - where camera can be placed will be cyclically be obscured by ground contact. Thus, implementation of several cameras is the only solution to provide continuous image acquiring of the forward path.
Other systems can be evaluated, such as the implementation of ultrasonic frequencies to deduce the external 3D environment and to perform obstacle detection.

Laboratory tests must be addressed to validate the effective functioning of the implemented control strategy. Analysing the behaviour of the actual plant, possible

integration of non-modelled aspects may arise.
Finally, both open-loop and closed-loop strategies will be tested. Open-loop can be imposed by modelling or adapting a physical joypad to the microcontroller signlas.

Bibliography

[1] Matteo Melchiorre et al. “Design of a Spherical UGV for Space Exploration”. In: vol. 2022-September. Cited by: 0. 2022. URL: https://www.scopus.com/inward/record.uri?eid=2-s2.0-85167585733&partnerID=40&md5=7854c22969fc85ad15057fc76712b44f.

[2] Colamartino Tommaso. *Design and Development of a Spherical Rover for Planetary Exploration*. webpage. URL: https://webthesis.biblio.polito.it/31455/.

[3] Seyed Amir Tafrishi et al. *Dynamical Behavior Investigation and Analysis of Novel Mechanism for Simulated Spherical Robot named ”RollRoller”*. 2016. arXiv: 1610.06218 [cs.RO].

[4] Maotao Yang et al. “Design and Analysis of a Spherical Robot with Two Degrees of Freedom Swing”. In: Aug. 2020, pp. 4913–4918. DOI: 10.1109/CCDC49329.2020.9164196.

[5] Sneha Gajbhiye and Ravi N. Banavar. “Geometric modeling and local controllability of a spherical mobile robot actuated by an internal pendulum”. In: *International Journal of Robust and Nonlinear Control* 26.11 (2016), pp. 2436–2454. DOI: https://doi.org/10.1002/rnc.3457. eprint: https://onlinelibrary.wiley.com/doi/pdf/10.1002/rnc.3457. URL: https://onlinelibrary.wiley.com/doi/abs/10.1002/rnc.3457.

[6] Mehdi Roozegar and Mohammad J. Mahjoob. “Modelling and control of a non-holonomic pendulum-driven spherical robot moving on an inclined plane: simulation and experimental results”. In: *IET Control Theory & Applications* 11.4 (2017), pp. 541–549. DOI: https://doi.org/10.1049/iet-cta.2016.0964. eprint: https://ietresearch.onlinelibrary.wiley.com/doi/pdf/

10.1049/iet-cta.2016.0964. URL: https://ietresearch.onlinelibrary.wiley.com/doi/abs/10.1049/iet-cta.2016.0964.

[7] Animesh Singhal et al. "Pendulum Actuated Spherical Robot: Dynamic Modeling Analysis for Wobble Precession". In: *IFAC-PapersOnLine* 55.22 (2022). 22nd IFAC Symposium on Automatic Control in Aerospace ACA 2022, pp. 67–72. ISSN: 2405-8963. DOI: https://doi.org/10.1016/j.ifacol.2023.03.012. URL: https://www.sciencedirect.com/science/article/pii/S2405896323002707.

[8] Mattias Seeman et al. "An Autonomous Spherical Robot for Security Tasks". In: Nov. 2006, pp. 51–55. DOI: 10.1109/CIHSPS.2006.313312.

[9] Angelo Pio Rossi et al. *DAEDALUS - Descent And Exploration in Deep Autonomy of Lava Underground Structures*. Mar. 2021. ISBN: 978-3-945459-33-1. DOI: 10.25972/OPUS-22791.

[10] Futao Wang et al. "Design and Analysis of a Spherical Robot with Rolling and Jumping Modes for Deep Space Exploration". In: *Machines* 10.2 (2022). ISSN: 2075-1702. DOI: 10.3390/machines10020126. URL: https://www.mdpi.com/2075-1702/10/2/126.

[11] Bo Zhao et al. "Dynamics and motion control of a two pendulums driven spherical robot". In: *2010 IEEE/RSJ International Conference on Intelligent Robots and Systems*. 2010, pp. 147–153. DOI: 10.1109/IROS.2010.5651154.

[12] Qiang Zhan, Yao Cai and Caixia Yan. "Design, analysis and experiments of an omni-directional spherical robot". In: *2011 IEEE International Conference on Robotics and Automation* (2011), pp. 4921–4926. URL: https://api.semanticscholar.org/CorpusID:13996599.

[13] Akash Singh et al. "Design and Motion Analysis of Complicant Omni-directional Spherical Modular Snake Robot (COSMOS)". In: June 2018.

[14] Jiazhen Chen et al. "Design and motion control of a spherical robot with control moment gyroscope". In: *2016 3rd International Conference on Systems and Informatics (ICSAI)*. 2016, pp. 114–120. DOI: 10.1109/ICSAI.2016.7810940.

[15] Shengju Sang et al. "Modeling and Simulation of a Spherical Mobile Robot". In: *Comput. Sci. Inf. Syst.* 7 (Feb. 2010), pp. 51–62. DOI: 10.2298/CSIS1001051S.

[16] Lianchao Jia et al. “The concept design of a mobile amphibious spherical robot for underwater operation”. In: *2016 IEEE International Conference on Cyber Technology in Automation, Control, and Intelligent Systems (CYBER)* (2016), pp. 411–415. URL: `https://api.semanticscholar.org/CorpusID:15954432`.

[17] Supaphon Kamon, Natthaphon Bunathuek and Pudit Laksanacharoen. “A Three-Legged Reconfigurable Spherical Robot No.3”. In: *2021 30th IEEE International Conference on Robot Human Interactive Communication (RO-MAN)*. 2021, pp. 426–433. DOI: `10.1109/RO-MAN50785.2021.9515319`.

[18] Takeshi Aoki et al. “Development of quadruped walking robot with spherical shell: improvement of climbing over a step”. In: *ROBOMECH Journal* 7 (May 2020). DOI: `10.1186/s40648-020-00170-5`.

[19] Jie Pan, ZhenYun Shi and TianMiao Wang. “Variable-model SMA-driven spherical robot”. In: *Science China Technological Sciences* 62 (July 2019), pp. 1–11. DOI: `10.1007/s11431-018-9408-3`.

[20] Maoxun Li et al. “Design and performance evaluation of an amphibious spherical robot”. In: *Robotics and Autonomous Systems* 64 (Nov. 2014). DOI: `10.1016/j.robot.2014.11.007`.

[21] Kuan-Yi Ho and N. Michael Mayer. “Implementation of a mobile spherical robot with shape-changed inflatable structures”. In: *2017 International Conference on Advanced Robotics and Intelligent Systems (ARIS)*. 2017, pp. 104–109. DOI: `10.1109/ARIS.2017.8297199`.

[22] Gregory C. Schroll. “Dynamic model of a spherical robot from first principles”. In: 2007. URL: `https://api.semanticscholar.org/CorpusID:126169560`.

[23] *Design and Path Planning for a Spherical Rolling Robot*. Vol. Volume 4A: Dynamics, Vibration and Control. ASME International Mechanical Engineering Congress and Exposition. Nov. 2013, V04AT04A028. DOI: `10.1115/IMECE2013-64994`. eprint: `https://asmedigitalcollection.asme.org/IMECE/proceedings-pdf/IMECE2013/56246/V04AT04A028/4229681/v04at04a028-imece2013-64994.pdf`. URL: `https://doi.org/10.1115/IMECE2013-64994`.

[24] Jia Qingxuan et al. "Motion control of a novel spherical robot equipped with a flywheel". In: *2009 IEEE International Conference on Information and Automation, ICIA 2009* (June 2009). DOI: 10.1109/ICINFA.2009.5205045.

[25] E. Potapov et al. "Developing Spherical Mobile Devices for Indoor Exploration". In: July 2020, pp. 1–4. DOI: 10.1109/SYNCHROINFO49631.2020.9166095.

[26] Wei-Jer Chang et al. "Design and implementation of a novel spherical robot with rolling and leaping capability". In: *Mechanism and Machine Theory* 171 (2022), p. 104747. ISSN: 0094-114X. DOI: https://doi.org/10.1016/j.mechmachtheory.2022.104747. URL: https://www.sciencedirect.com/science/article/pii/S0094114X22000246.

[27] Yangyang Dong et al. "Spherical robot with spring energy storage type hopping mechanisms: design, dynamics and experimental evaluation". In: *Ind. Robot* 49 (2022), pp. 760–769. URL: https://api.semanticscholar.org/CorpusID:247331901.

[28] Christopher Dudley, Alexander Woods and Kam Leang. "A micro spherical rolling and flying robot". In: Sept. 2015, pp. 5863–5869. DOI: 10.1109/IROS.2015.7354210.

[29] Sahand Sab et al. "Rollocopter: An Energy-Aware Hybrid Aerial-Ground Mobility for Extreme Terrains". In: Mar. 2019, pp. 1–8. DOI: 10.1109/AERO.2019.8741685.

[30] Liwei Shi et al. "A Fuzzy PID Algorithm for a Novel Miniature Spherical Robots with Three-dimensional Underwater Motion Control". In: *Journal of Bionic Engineering* 17 (Aug. 2020). DOI: 10.1007/s42235-020-0087-3.

[31] Tuanjie Li and Wei-Guang Liu. "Design and Analysis of a Wind-Driven Spherical Robot with Multiple Shapes for Environment Exploration". In: *Journal of Aerospace Engineering* 24 (2011), pp. 135–139. URL: https://api.semanticscholar.org/CorpusID:109997448.

[32] Shuoxin Gu, Shuxiang Guo and Zheng Liang. "A highly stable and efficient spherical underwater robot with hybrid propulsion devices". In: *Autonomous Robots* 44 (May 2020). DOI: 10.1007/s10514-019-09895-8.

[33] Maxon Motor. *Maxon RE 40 Datasheet*. Accessed: 2024-07-10. 2022. URL: https://www.maxongroup.it/medias/sys_master/root/8992314425374/EN-22-159.pdf.

[34] Maxon Motor. *GP 42 C Gearhead Datasheet*. Datasheet for Maxon GP 42 C Gearhead. 2024. URL: https://www.maxongroup.com/medias/sys_master/root/8882781224990/EN-21-405-406-407.pdf%202021.

[35] Maxon Motor AG. *ESCON 50/5 Servo Controller*. Datasheet. 2018. URL: https://www.maxongroup.ch/medias/sys_master/root/8834332459038/409510-ESCON-50-5-Manuale-di-riferimento-It.pdf.

[36] Maxon Motor AG. *HEDL 5540 Encoder*. Datasheet. 2021. URL: https://www.maxongroup.com/medias/sys_master/root/8884124516382/EN-21-488-492.pdf.

[37] Maxon Motor AG. *Maxon DCX 35L Motor Datasheet*. https://www.maxongroup.com/medias/sys$_m$
$22 - 114$.*pdf* 2022. Accessed: 2024-07-10. 2023.

[38] Infineon Technologies AG. *BTS7960 High Current Motor Driver*. Datasheet. 2024. URL: https://www.handsontec.com/dataspecs/module/BTS7960%20Motor%20Driver.pdf.

[39] StepperOnline. *NEMA 17 Stepper Motor Datasheet*. Datasheet for 40Ncm torque stepper motor. 2024. URL: https://www.gotronic.fr/pj2-31116-17hs15-0404s-2565.pdf.

[40] FYSETC. *TMC2208 Information*. Accessed: 2023-07-15. 2023. URL: https://wiki.fysetc.com/TMC2208/.

[41] ams AG. *AS5600: Programmable Contactless Potentiometer*. Datasheet. 2018. URL: https://www.mouser.com/datasheet/2/588/AS5600_DS000365_5-00-1877365.pdf.

[42] Components101. *MPU6050 Module*. Accessed: 2023-07-15. 2023. URL: https://components101.com/sensors/mpu6050-module.

[43] Senring. *Bore Slip Ring H1532 Datasheet*. https://www.senring.com/through-hole-slip-ring/small-hole/h1532.html. Accessed: 2024-07-10. 2023.

[44] Components101. *NRF24L01 Pinout, Features & Datasheet*. Accessed: 2023-07-15. 2023. URL: https://components101.com/wireless/nrf24l01-pinout-features-datasheet.

[45] *DIY Arduino RC Transmitter*. webpage. URL: https://howtomechatronics.com/projects/diy-arduino-rc-transmitter/.

[46] Arduino. *Arduino Mega 2560 Rev3*. Datasheet. 2024. URL: https://docs.arduino.cc/resources/datasheets/A000067-datasheet.pdf.

[47] Max Amps. *Max Amps MA-5000-8s-Li-ion-Pack*. Datasheet. 2024. URL: https://cdn.shopify.com/s/files/1/0609/0811/0079/files/MaxAmps_5000_8S_Li-ion_Data_sheet.pdf?v=1707862130.